

1 **Post hoc Uncertainty Quantification for Remote Sensing Observing Systems** \*2 Amy Braverman<sup>††</sup>, Jonathan Hobbs<sup>†</sup>, Joaquim Teixeira<sup>†</sup>, and Michael Gunson<sup>†</sup>

3

4 **Abstract.** This article sets forth a practical methodology for uncertainty quantification of physical state estimates derived from remote sensing observing systems. Remote sensing instruments observe parts of the electromagnetic spectrum and use computational algorithms to infer the underlying true physical states. In current practice, many sources of uncertainty are not accounted for in this process, leading to underestimates of uncertainties on quantities of interest. We propose a procedure that combines Monte Carlo simulation experiments with statistical modeling to approximate distributions of unknown true states given point estimates of those states. Our method is carried out post hoc; that is after the operational processing step. We demonstrate the procedure using four months of data from NASA’s Orbiting Carbon Observatory-2 mission and compare to validation measurements from the Total Column Carbon Observing Network.

14 **Key words.** Uncertainty quantification, bootstrap bias correction, remote sensing, Gaussian mixture modeling, Orbiting Carbon Observatory-2 mission.

16 **AMS subject classifications.** 62G05, 62G07, 62G08, 62G15

17 **1. Introduction.** The ability of space-borne remote sensing observations to address im-  
 18 portant Earth and climate science problems rests crucially on how well geophysical quantities  
 19 of interest (QOIs) can be inferred from these data. Observing systems that collect and process  
 20 this information must address uncertainties arising not only from measurement errors, but also  
 21 from imperfect physical models and their parameters, computational artifacts, and potentially  
 22 other unknowns that affect the conversion of observations to QOI estimates. While much of  
 23 this sounds familiar in the context of the Uncertainty Quantification discipline [32], existing  
 24 techniques do not address the problem in a practical way that can be applied comprehensively  
 25 to very large data sets produced in routine operations.

26 A remote sensing observing system is an infrastructure that senses electromagnetic energy  
 27 and converts it into estimates of nature’s true states. In this paper, we consider a system in  
 28 which observations are collected over different wavelengths as a spectrum of measured radi-  
 29 ances. These spectra carry information about the properties of the Earth’s atmosphere and  
 30 surface, as encountered in each individual observational unit corresponding to a specific ground  
 31 footprint (also sometimes called a “sounding”), because photons at different wavelengths are  
 32 scattered and absorbed in characteristic ways, depending on the make-up, function, and prop-  
 33 erties of physical constituents with which photons interact. Inference about QOIs from a noisy  
 34 radiance spectra is a fundamental problem of remote sensing science. It requires knowledge  
 35 of the physics of radiative transfer [4], and substantial computational resources, especially  
 36 for operational satellite systems which can return terabytes of data per day corresponding to  
 37 millions of cases. In nearly all cases, there are only a few, sparse measurements from surface or

---

\*Submitted to the editors December 4, 2019.

**Funding:** This work was performed at the Jet Propulsion Laboratory, California Institute of Technology, under contract with the National Aeronautics and Space Administration.

<sup>†</sup>Jet Propulsion Laboratory, California Institute of Technology ([Amy.Braverman@jpl.nasa.gov](mailto:Amy.Braverman@jpl.nasa.gov))

38 aircraft instruments with which to validate or calibrate the satellite measurements, and these  
39 corroborating data also come with their own uncertainties. Finally, for most existing missions,  
40 uncertainty quantification must be done post hoc without rerunning computationally costly  
41 data processing algorithms.

42 Various authors have addressed the problem of uncertainties in satellite derived estimates  
43 of geophysical QOIs. Some papers (e.g., [31, 39, 51]) qualify as a general call to arms. Others  
44 such as [1, 20, 27] use ground-based validation data in highly restricted case studies to ascertain  
45 error characteristics under specific conditions. Numerous other examples can be found in  
46 [51]. For operational missions, [37, 36] used the linear sensitivity (first derivative) of the  
47 forward radiative transfer model to propagate radiance measurement error forward through  
48 their computations. Unlike the case-study-based methods, this method is applied in a way that  
49 produces, in principle, a nominal variance for each and every sounding. [30] used a Monte Carlo  
50 simulation to quantify uncertainty of their estimates without assuming linearity. However, this  
51 analysis was performed only after aggregating to coarse spatial resolution, and only addressed  
52 uncertainty due to geographic sampling issues and to several specific methodological choices  
53 implemented in their processing stream.

54 More recently, Bayesian methods have become popular, as they produce probability distri-  
55 butions of the QOI given the observed quantities rather than point estimates alone. Markov  
56 chain Monte Carlo (MCMC) is sometimes used in small applications and case studies (e.g.,  
57 [18, 38, 3, 24]). MCMC is too computationally intensive for routine operational use though.  
58 Instead, “optimal estimation” (OE) [42, 43] has been widely adopted as the de facto state-  
59 of-the-art (e.g., [52, 21, 25, 50]). OE is a computational implementation of Bayes Rule that  
60 produces (implied Gaussian) probability distributions for true QOIs given radiances.

61 Some argue that OE automatically achieves uncertainty quantification [50] because it pro-  
62 duces output that can be interpreted as the moments of a distribution. However, operational  
63 implementations and limited physical knowledge result in uncertainties that impact the reli-  
64 ability of OE itself. For example, while the equations of radiative transfer are relatively well  
65 understood, operational codes must run quickly and usually approximate some processes (or  
66 indeed ignore them completely). Tables of spectroscopic information that describe spectral  
67 absorption patterns induced by different gases, and sensitivities of detectors and other parts  
68 of the optical system, are derived from ground-based experiments. All are assumed fixed  
69 and known, even though they are uncertain. Even the discretizations of continuous physical  
70 quantities that define the state and radiance vectors, the grids used by numerical solvers, and  
71 the optimization routines used to solve for the QOI can induce uncertainty, both individually  
72 and as a result of high-order interactions.

73 Neither OE nor earlier approaches quantify total uncertainty on a sounding by sounding  
74 basis. They do not quantify total uncertainty because they rely on enumeration of specific  
75 known source of uncertainty to be propagated, and do not include the elusive unknown un-  
76 knowns. These methods cannot be applied on a sounding-by-sounding basis because they  
77 require ground truth validation data that are not universally available. In this article, we  
78 propose a new method for estimating probability distributions for QOIs that is free of these  
79 restrictions. We derive conditional distributions of the QOI, given the operational point es-  
80 timates, by fitting the parameters of a Gaussian mixture regression model to an ensemble of  
81 simulated true and estimated states. Then, we use the fitted mixture of regression functions to

82 define the desired conditional distributions by plugging in sounding-specific operational point  
83 estimates as predictors. This is a “top-down” approach that does not require enumeration of  
84 individual uncertainty sources. Once the parameters of the Gaussian mixture are fitted, it is  
85 fast and easy to compute the sounding-specific conditional distributions.

86 Our method can be seen as a modified and extended version of the the bootstrap bias  
87 correction [12, 10, 23]. There, one starts with a single sample, and draws a set of resamples  
88 from it. The statistic of interest is computed from the original sample, and from the resamples.  
89 The discrepancy between (the mean of) the resampled statistics and the original statistic is  
90 used as a proxy for the relationship between the original statistic and the true parameter.  
91 Here, our analog of the resamples is a simulated joint ensemble of true and estimated QOIs.  
92 However, we go beyond correcting for bias alone with two innovations. The first is that  
93 we derive approximations for the full conditional distributions of the true states given the  
94 operational state estimates. The second is that we use both the simulated and operationally-  
95 derived information together to approximate forward model discrepancy and account for it  
96 as part of total uncertainty. As far as we know there are no comparable methods in either  
97 the uncertainty quantification or remote sensing literature that deliver such comprehensive  
98 probabilistic descriptions of uncertainties associated with operational remote sensing state  
99 estimates.

100 To demonstrate and evaluate our methodology, we apply it to data from NASA’s Orbiting  
101 Carbon Observatory-2 (OCO-2) mission. See [6] for an overview of the mission and statistical  
102 issues surrounding its processing and scientific value. OCO-2 uses OE to infer the distribu-  
103 tion of its primary QOI, total column mole-fraction of CO<sub>2</sub> (known as XCO<sub>2</sub> in the remote  
104 sensing community) by sounding. While our method is equally applicable to vector-valued  
105 QOIs, XCO<sub>2</sub> is a scalar quantity; this simplifies visualization and analysis. Another reason to  
106 highlight OCO-2 is its stringent uncertainty requirements. The primary scientific application  
107 of OCO-2’s estimates is as input to flux inversion (data assimilation) models [17, 35, 49] that  
108 estimate the exchange of carbon between Earth’s surface and atmosphere. Determination of  
109 flux requires CO<sub>2</sub> estimates with high accuracy (less than 0.3 parts per million (ppm) in scenes  
110 with background levels of around 410 ppm), and high precision (standard errors less than 0.5  
111 ppm). Consequently, uncertainty quantification has been a major focus of the OCO-2 science  
112 endeavor.

113 Members of the OCO-2 team have performed various studies that attempt to quantify  
114 uncertainties in its retrieved estimates (e.g., [5, 53]). However, many of these stay wholly  
115 within the optimal estimation, linear Gaussian framework, and are therefore not able to assess  
116 uncertainties due to failure of those assumptions. Alternatively, Cressie and co-authors [7, 8]  
117 investigated the impact of non-linearity of the forward model on both mean and variance  
118 estimates produced by OE. These analyses yield valuable insights into the performance of  
119 OE, but do not represent an attempt to evaluate or quantify total uncertainty expressed by  
120 operationally-derived distributions.

121 The remainder of this article is organized as follows. First, we articulate our reference  
122 statistical model for remote sensing observing systems (Section 2), and then the methodology  
123 for estimating conditional distributions of true states given their point estimates (Section  
124 3). In Section 4 we describe how we tailor our method for the case of OCO-2, and evaluate  
125 the results through comparisons with available ground truth information. The final section

126 contains a summary and discussion.

127 **2. Statistical model of an observing system and its output.** An observing system rep-  
 128 presents the flow of information from nature, which produces the quantities of interest, to the  
 129 space-borne hardware that collects radiances, and finally to the software that performs esti-  
 130 mation of the QOIs from these observations. Consider Figure 1. The state vector is  $\mathbf{X} =$   
 $(X_1, X_2, \dots, X_{L_X})'$  and it, or some part of it, usually is the quantity of interest. Nature's for-

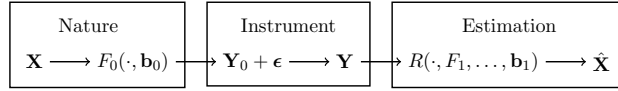


Figure 1. Schematic diagram of a generic observing system.

131 ward function,  $F_0$ , converts  $\mathbf{X}$  into the noiseless radiance vector,  $\mathbf{Y}_0 = (Y_{01}, Y_{02}, \dots, Y_{0L_Y})'$ ,  
 132 which is observed by the remote sensing instrument with measurement error  $\epsilon$  (also of di-  
 133 mension  $L_Y$ ). The forward function also typically depends on an additional set of variables,  
 134 denoted by  $\mathbf{b}_0$ , that are not part of the state vector but nonetheless influence the transfor-  
 135 mation of the state into noiseless radiances; e.g., spectroscopic absorption coefficients that  
 136 characterize various atmospheric constituents. The distinction between  $F_0$  and  $\mathbf{b}_0$  is an aca-  
 137 demic one because they are confounded components of our model of nature, rather than  
 138 properties of nature itself. Since they can't be decoupled, we will always refer to them as a  
 139 unit,  $F_0(\cdot, \mathbf{b}_0)$ .

141 The noisy radiance vector,  $\mathbf{Y} = \mathbf{Y}_0 + \epsilon$  is ingested into the retrieval algorithm— so-named  
 142 because it retrieves the true state from the observations— to produce a point estimate of the  
 143 true state, denoted by  $\hat{\mathbf{X}}$  in the figure. In OE,  $\hat{\mathbf{X}}$  can be interpreted as a conditional mean, and  
 144 is accompanied by an estimate of the covariance matrix obtained via a linear approximation  
 145 to the forward function.

146 The retrieval algorithm depends on a forward model,  $F_1$ , and its corresponding forward  
 147 model parameters,  $\mathbf{b}_1$ , which are the best known practical approximations to  $F_0$  and  $\mathbf{b}_0$ ,  
 148 respectively. Arguably,  $F_1$  and  $\mathbf{b}_1$  may be considered distinct, with  $F_1$  being implemented  
 149 as algorithm computer code and  $\mathbf{b}_1$  being a set of fixed, ancillary inputs provided to  $F_1$   
 150 in addition to the radiances. The ellipses in the arguments to  $R$  in Figure 1 represent other  
 151 required choices that must be made in order to run the retrieval algorithm code, and will affect  
 152 the quality of the estimates. We call these “settings”. Examples include convergence criteria,  
 153 the grid over which the algorithm will solve for the required optimum, etc. For compactness,  
 154 we subsume settings into  $\mathbf{b}_1$ . Despite their potential separation in implementation, we consider  
 155  $F_1(\cdot, \mathbf{b}_1)$  to be a unit, as is the case with  $F_0(\cdot, \mathbf{b}_0)$ .

156 From an uncertainty quantification perspective, one might view  $\mathbf{Y}$  as the primary input  
 157 to a deterministic function  $R$ , and  $\hat{\mathbf{X}}$  as the output for which uncertainty is to be quantified.  
 158 In that case, we equate  $\hat{\mathbf{X}}$  with some measure of location of  $P(\mathbf{X}|\mathbf{Y})$ . Alternatively, one  
 159 might view  $\mathbf{X}$ , though not directly observed, as the input to the composite system that  
 160 includes nature, the instrument, and the retrieval process. From this point of view, we seek  
 161 the conditional distribution  $P(\mathbf{X}|\hat{\mathbf{X}})$ . This distribution reflects the uncertainty about  $\mathbf{X}$  that  
 162 remains after seeing  $\hat{\mathbf{X}}$ .

163 The retrieval community takes the first perspective:  $F_1$  is fixed, and  $\mathbf{b}_1$  is set by ad

164 hoc testing of different candidate values according to knowledge of the underlying physics.  
 165 Comparisons of resulting values of  $\hat{\mathbf{X}}$  to ground truth, where available, dictate the final fixed  
 166 value of  $\mathbf{b}_1$ . The only source of uncertainty accounted for is that of the input radiance vector,  
 167  $\mathbf{Y}$ . By treating  $F_1(\cdot, \mathbf{b}_1)$  as fixed, this procedure ignores the impact of uncertainties that may  
 168 be induced by their misspecification. [19] showed that misspecifications of this sort can lead  
 169 to both bias and variance in the retrieved quantities through unpredictable interactions and  
 170 algorithm artifacts.

171 Our perspective is that the uncertainty to be quantified is that of the entire, end-to-end  
 172 observing system shown in Figure 1, and so our goal is to provide the conditional distribution  
 173  $P(\mathbf{X}|\hat{\mathbf{X}})$ . For each  $\hat{\mathbf{X}}$  we approximate  $P(\mathbf{X}|\hat{\mathbf{X}})$  via a Gaussian mixture model (GMM) in which  
 174 the component-wise means, variances, and mixing probabilities are functions of the realized  
 175 value of  $\hat{\mathbf{X}}$ . Those functions are estimated from a simulation experiment that 1) incorporates  
 176 a model discrepancy term to account for structural and parametric model uncertainty, and  
 177 2) borrows strength over a representative ensemble of synthetic state vectors to account for  
 178 the range of conditions to which the model must apply. The simulation experiment allows us  
 179 to quantify the aggregate impact of uncertainties due to both known and unknown sources  
 180 because we know the “truth”. Once the parameters of the GMM are estimated, the conditional  
 181 distributions of the true states given actual retrieved estimates are obtained by plugging the  
 182 retrieved values into the estimated regression equations. This method is applicable regardless  
 183 of whether  $\hat{\mathbf{X}}$  is a least squares, OE, or any other type of estimate.

184 The approach requires that we simulate a realistic ensemble of synthetic true states and  
 185 generate corresponding ensembles of radiances and retrieved state estimates. The simulated  
 186 true state ensemble need not be identical to nature’s true ensemble, just realistic in the sense  
 187 that it spans the range of plausible true states the observing system is likely to encounter.  
 188 Procedures for creating this ensemble will vary by application and even by analyst since  
 189 “plausible” is subjective. Likewise, the forward propagation of the ensemble through  $F_0(\cdot, \mathbf{b}_0)$   
 190 in the simulation, is application and analyst-specific since nature’s true forward function is  
 191 unknown, but must be represented in some way and be distinct from  $F_1(\cdot, \mathbf{b}_1)$ . In Section 4,  
 192 we demonstrate our solutions to these problems for OCO-2.

193 We stress that a major restriction on our work for OCO-2 and for other existing missions  
 194 is that UQ must be performed *post hoc*. The design and implementation of the operational  
 195 retrieval algorithm cannot be changed nor can it be interfered with. Uncertainty quantification  
 196 must be after the fact. Consequently, our goal here is only to obtain an honest estimate of  
 197 total uncertainty, not to break it down into contributing factors or to reduce it.

198 Our framework uses the following statistical model based on Figure 1.

$$199 \quad \mathbf{X} \sim P_{\mathbf{X}}(\mathbf{x}; \boldsymbol{\theta}_{\mathbf{X}}), \quad \mathbf{Y}_0 = F_0(\mathbf{X}, \mathbf{b}_0), \quad \mathbf{Y} = \mathbf{Y}_0 + \boldsymbol{\epsilon}, \quad \boldsymbol{\epsilon} \sim \text{MVN}(\mathbf{0}, \boldsymbol{\Sigma}_{\boldsymbol{\epsilon}}),$$

$$200 \quad (2.1) \quad \boldsymbol{\theta}_{\mathbf{X}} = \{\boldsymbol{\mu}_{\mathbf{X}}, \boldsymbol{\Sigma}_{\mathbf{X}}, \dots\}, \quad \text{and} \quad \hat{\mathbf{X}}(\mathbf{Y}, \mathbf{b}_1) = R(\mathbf{Y}, F_1, \mathbf{b}_1).$$

202 All variables in bold are column vectors or matrices, except  $\boldsymbol{\theta}_{\mathbf{X}}$  which denotes a set of param-  
 203 eters. The dimensions of  $\mathbf{X}$ ,  $\boldsymbol{\mu}_{\mathbf{X}}$  and  $\hat{\mathbf{X}}$  are  $L_{\mathbf{X}} \times 1$ . The dimensions of  $\mathbf{Y}_0$ ,  $\mathbf{Y}$ ,  $\boldsymbol{\epsilon}$ , and the zero  
 204 vector are  $L_{\mathbf{Y}} \times 1$ . The matrix  $\boldsymbol{\Sigma}_{\mathbf{X}}$  is of dimension  $L_{\mathbf{X}} \times L_{\mathbf{X}}$ , and  $\boldsymbol{\Sigma}_{\boldsymbol{\epsilon}}$  and is  $L_{\mathbf{Y}} \times L_{\mathbf{Y}}$ . The  
 205 vector  $\mathbf{b}_0$  contains both known and unknown quantities set by nature, and has unspecified  
 206 length. Finally,  $\mathbf{b}_1$  is a fixed, known column vector containing all parameters necessary to run

207 the retrieval.

208 This model prescribes that nature draws a true state vector from  $P_{\mathbf{X}}$  having parameter  
 209 vector  $\theta_{\mathbf{X}}$ . From the standpoint of the retrieval algorithm, the true state, its distribution, and  
 210 the measurement error  $\epsilon$ , are all unknown. We will, however, assume that the statistics of  $\epsilon$  are  
 211 known, as would be the case from pre-launch calibration studies. Radiance measurement errors  
 212 are assumed to be multivariate normal with zero mean and known covariance matrix  $\Sigma_{\epsilon}$ . The  
 213 only input to  $R$  subject to randomness in Equation (2.1) is therefore  $\mathbf{Y}$ . All other quantities  
 214 on which  $R$  depends are fixed at nominal values using expert judgement and modified, if  
 215 necessary, to conform to computational requirements.

216 **3. Approach and methods.** The foundation of our approach is the statistical model given  
 217 by Equation (2.1), overlaid with our view that the computational machinery of the observing  
 218 system is a complex estimator who's performance is summarized by  $P(\mathbf{X}|\hat{\mathbf{X}})$ . This condi-  
 219 tional distribution may be derived from the joint distribution  $P(\mathbf{X}, \hat{\mathbf{X}})$ , which contains all the  
 220 information about the uncertainty  $\hat{\mathbf{X}}$  as an estimate of  $\mathbf{X}$  [11, 48]. Since we do not know the  
 221 true joint distribution, we appeal to resampling to provide a synthetic ensemble that is our  
 222 best empirical representation of it.

223 **3.1. Methodology.** Our general strategy is summarized in Figure 2. The first row of this  
 224 flowchart roughly mirrors Figure 1, but with a number of important modifications. First,  $\tilde{P}$   
 225 plays the role of nature. An ensemble of simulated true states are drawn from it. This set  
 226 of  $M$  simulated state vectors is the  $(M \times L_{\mathbf{X}})$  data matrix,  $\{\mathbf{X}_m^{\text{sim}}\}_{m=1}^M \equiv (\mathbf{X}_1^{\text{sim}}, \dots, \mathbf{X}_M^{\text{sim}})'$ ,  
 227 and we call it the synthetic true state ensemble. It represents a set of plausible, alternative  
 228 realizations of the state vector that the observing system is likely to encounter. We will usually  
 229 suppress the indices on the bracket notation for brevity.

230 Second, Figure 1 shows that the state vector is converted by nature's true forward func-  
 231 tion,  $F_0(\cdot, \mathbf{b}_0)$ , into a noiseless radiance,  $\mathbf{Y}_0$ , which is then observed by the instrument with  
 232 measurement error  $\epsilon$ . Figure 2 shows the transformation by the forward *model*,  $F_1(\cdot, \mathbf{b}_1)$ . This  
 233 is because in practice we do not know nature's true forward function; all we have is our best  
 234 forward model which will also be used in the retrieval process in the second row of Figure 2.

235 It is overly optimistic to assume that the forward model used in the retrieval is identical  
 236 to nature's true forward function. To compensate, we add an extra component of noise to  
 237 the synthetic, noiseless radiance ensemble  $\{\mathbf{Y}_0^{\text{sim}}\}$ , as shown in the right-most box on the  
 238 first row of Figure 2. This model discrepancy term is  $\delta^{\text{sim}}$  and is an independent draw from a  
 239 multivariate Gaussian distribution with mean vector and covariance matrix that are estimated  
 240 off-line from *spectral residuals* that can be produced by any retrieval algorithm, and by our  
 241 simulation. Spectral residuals are the differences between the observed radiances and the  
 242 radiances implied by the forward model, evaluated at the converged estimate of the state.  
 243 Section 4.1.4 and Appendix C describe how we estimate the mean vector and covariance  
 244 matrix of the distribution of  $\delta^{\text{sim}}$  from the ensembles of available spectral residuals.

245 The second row of Figure 2 shows how the simulated noisy radiance ensemble,  $\{\mathbf{Y}^{\text{sim}}\}$ , is  
 246 input to the retrieval algorithm to produce the corresponding retrieved estimates. We form  
 247 a synthetic training ensemble by pairing each simulated true state with its corresponding  
 248 retrieval:  $\{\mathbf{X}^{\text{sim}}, \hat{\mathbf{X}}^{\text{sim}}\}$ . Then, we fit a Gaussian mixture model to this set, and subsequently

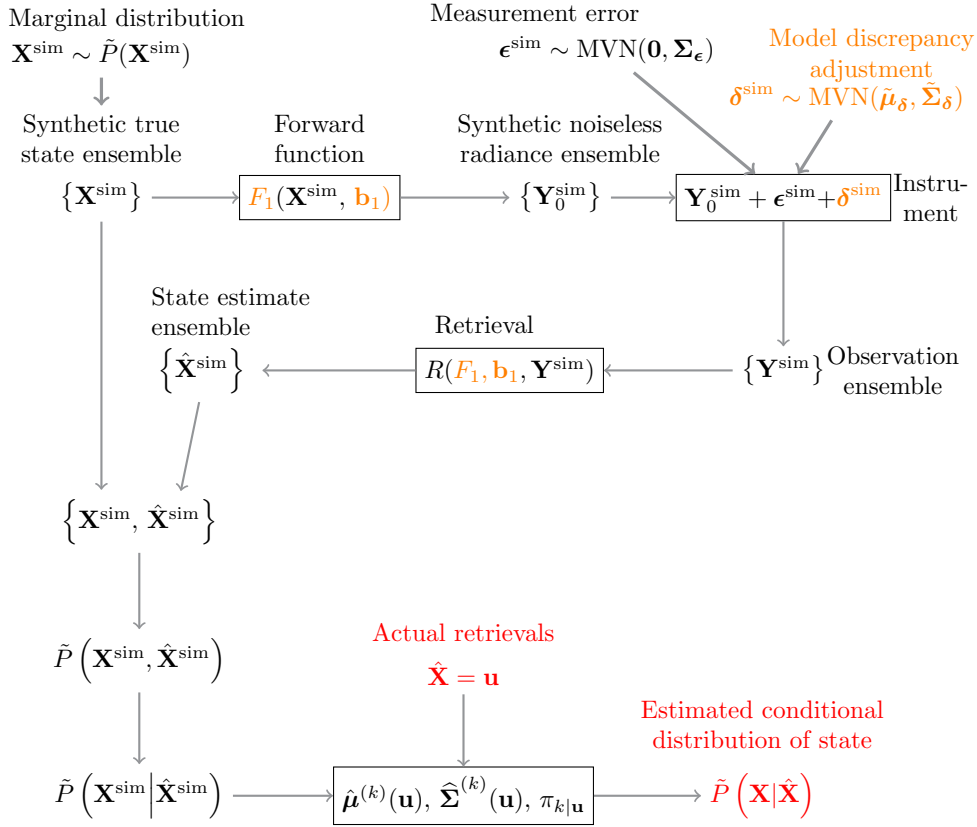


Figure 2. Conceptual diagram of the uncertainty quantification strategy.

249 derive 1) regression mean and variance functions for each mixture component, and 2) the  
 250 conditional probabilities of component membership given the value of the predictors,  $\hat{\mathbf{X}}$ . Once  
 251 these functions are estimated from the simulated ensemble, any new or operationally retrieved  
 252 state estimate can serve as a predictor. We simply plug the predictor into the regression  
 253 equations to obtain parameters of the Gaussian mixture component conditional distributions,  
 254 and the conditional probability of component membership.

255 The next subsection briefly reviews Gaussian mixture models, and the software we use for  
 256 fitting them.

257 **3.2. Gaussian mixture models and software to fit them.** The Gaussian mixture density  
 258 for a multivariate random vector  $\mathbf{V}$  is,

$$259 \quad (3.1) \quad f_{\mathbf{V}}(\mathbf{v}) = \sum_{k=1}^K \pi_k \phi(\mathbf{v}; \boldsymbol{\mu}_k, \Sigma_k), \quad \sum_{k=1}^K \pi_k = 1,$$

260

261 where  $\phi(\mathbf{v}; \boldsymbol{\mu}_k, \Sigma_k)$  is the multivariate normal density function with mean vector  $\boldsymbol{\mu}_k$  and  
 262 covariance matrix  $\Sigma_k$ , evaluated at  $\mathbf{v}$ ;  $\pi_k$  is the (mixing) weight of component  $k$ , and  $K$  is

263 the total number of components [29]. We abbreviate this density by,

$$264 \quad (3.2) \quad \mathbf{V} \sim \text{GMM} \left( K, \{ \boldsymbol{\mu}_k, \boldsymbol{\Sigma}_k, \pi_k \}_{k=1}^K \right).$$

266 Given a sample,  $\mathbf{V}_1, \dots, \mathbf{V}_N$ , the maximum likelihood estimates of the parameters of the  
267 model specified Equation (3.2) are,

$$268 \quad (3.2) \quad \left\{ \widehat{K}, \widehat{\boldsymbol{\mu}}_1, \dots, \widehat{\boldsymbol{\mu}}_{\widehat{K}}, \widehat{\boldsymbol{\Sigma}}_1, \dots, \widehat{\boldsymbol{\Sigma}}_{\widehat{K}}, \widehat{\pi}_1, \dots, \widehat{\pi}_{\widehat{K}} \right\}.$$

270 R's *densityMclust* function in the package *mclust* [47, 16] provides software for estimating  
271 these parameters. In addition, *densityMclust* returns another object that is key for our  
272 purposes. It is an  $N \times \widehat{K}$  matrix of conditional probabilities,

$$273 \quad (3.3) \quad \widehat{\pi}_{k|\mathbf{v}_n} = \tilde{P}(\kappa_n = k | \mathbf{V} = \mathbf{v}_n) = \frac{\widehat{\pi}_k \phi(\mathbf{v}_n; \widehat{\boldsymbol{\mu}}_k, \widehat{\boldsymbol{\Sigma}}_k)}{\sum_{l=1}^{\widehat{K}} \widehat{\pi}_l \phi(\mathbf{v}_n; \widehat{\boldsymbol{\mu}}_l, \widehat{\boldsymbol{\Sigma}}_l)},$$

275 for  $k = 1, \dots, \widehat{K}, n = 1, \dots, N$ . Here,  $\kappa_n$  is a random variable that indicates component  
276 membership: the probability that  $\mathbf{V}_n$  comes from component  $k$  is  $\widehat{\pi}_k$  before observing  $\mathbf{V}_n$ ,  
277 and  $\widehat{\pi}_{k|\mathbf{v}_n}$  after seeing  $\mathbf{V}_n = \mathbf{v}_n$  [48].

278 Equation (3.3) is, in some ways, the most fundamental quantity returned by this software.  
279 It provides a probabilistic mapping of the  $\mathbf{V}_n$  to the  $\widehat{K}$  Gaussian components of the model.  
280 This is critical if, say, one fits the model to standardized data but wants to report the result on  
281 the raw scale. For example, suppose  $\mathbf{V}_n$  is partitioned into two sub-vectors that are measured  
282 on very different scales so one would influence the calculation disproportionately if a model  
283 was fitted to the raw data. Suppose  $\mathbf{V}$  is  $d_{\mathbf{V}}$ -dimensional, and let  $\mathbf{V}_n = (\mathbf{W}'_n, \mathbf{U}'_n)'$ , where  
284  $\mathbf{W}$  is  $d_{\mathbf{W}}$ -dimensional, and  $\mathbf{U}$  is  $d_{\mathbf{U}}$ -dimensional, and  $d_{\mathbf{V}} = d_{\mathbf{W}} + d_{\mathbf{U}}$ . It would make sense to  
285 fit the model to standardized versions of these variables by converting  $\mathbf{W}_n$  to  $\mathbf{Z}_{1n}$  and  $\mathbf{U}_n$  to  
286  $\mathbf{Z}_{2n}$ :

$$287 \quad (3.4) \quad \mathbf{Z}_{1n} = (\mathbf{W}_n - \mathbf{m}_{\mathbf{W}})' \mathbf{C}_{\mathbf{W}}^{-1/2} \quad \text{and} \quad \mathbf{Z}_{2n} = (\mathbf{U}_n - \mathbf{m}_{\mathbf{U}})' \mathbf{C}_{\mathbf{U}}^{-1/2},$$

289 where  $\mathbf{m}_{\mathbf{W}}$  and  $\mathbf{C}_{\mathbf{W}}$  are the mean vector and covariance matrix of  $\mathbf{W}_1, \dots, \mathbf{W}_N$ , and  $\mathbf{m}_{\mathbf{U}}$   
290 and  $\mathbf{C}_{\mathbf{U}}$  are defined similarly. Denote the standardized vector  $\mathbf{V}_n = (\mathbf{Z}'_{1n}, \mathbf{Z}'_{2n})'$ , and fit a  
291 GMM to  $\mathbf{V}_1, \mathbf{V}_2, \dots, \mathbf{V}_N$ . Estimates of the component mean vectors and covariance matrices  
292 are on the standard scale ( $\widehat{\boldsymbol{\mu}}_k$  and  $\widehat{\boldsymbol{\Sigma}}_k$ ), but can easily be recomputed from the raw data by  
293 calculating weighted averages and variances using the  $\widehat{\pi}_{k|\mathbf{v}_n}$  as weights:

$$294 \quad (3.5) \quad \widehat{\boldsymbol{\mu}}_k = \sum_{n=1}^N \mathbf{v}_n \left[ \frac{\widehat{\pi}_{k|\mathbf{v}_n}}{\sum_{m=1}^N \widehat{\pi}_{k|\mathbf{v}_m}} \right],$$

$$295 \quad (3.6) \quad \widehat{\boldsymbol{\Sigma}}_k = \sum_{n=1}^N (\mathbf{v}_n - \widehat{\boldsymbol{\mu}}_k) (\mathbf{v}_n - \widehat{\boldsymbol{\mu}}_k)' \left[ \frac{\widehat{\pi}_{k|\mathbf{v}_n}}{\sum_{m=1}^N \widehat{\pi}_{k|\mathbf{v}_m}} \right].$$

297 In practice we will use R's *weighted.mean* function to compute  $\widehat{\boldsymbol{\mu}}_k$ , and the *cov.shrink* func-  
298 tion from the package *corpcor* [45] to compute shrinkage estimates of  $\boldsymbol{\Sigma}_k$ .

299 The idea can be extended to other convenient transformations beyond simple standard-  
 300 ization. In particular, if the dimension of  $\mathbf{V}$  is large, *densityMclust* can be slow. In that  
 301 case,  $\mathbf{V}_1, \mathbf{V}_2, \dots, \mathbf{V}_N$  may be further transformed by projecting them into the space spanned  
 302 by the leading principal components of  $\mathbf{V}$  estimated from the (standardized) data. Let  $\mathbf{C}_\mathbf{Y}$   
 303 be the (empirical) covariance matrix of  $\mathbf{V}_1, \mathbf{V}_2, \dots, \mathbf{V}_N$ , and let  $\mathbf{E}_i$  be the  $i$ -th eigenvector  
 304 of  $\mathbf{C}_\mathbf{Y}$ . The eigenvectors are arranged in order corresponding to the order of their descend-  
 305 ing eigenvalues,  $\lambda_1, \lambda_2, \dots, \lambda_{d_\mathbf{V}}$ . The leading eigenvector matrix of  $\mathbf{C}_\mathbf{Y}$  is  $\mathbf{E}$ , with columns  
 306  $\mathbf{E}_1, \mathbf{E}_2, \dots, \mathbf{E}_l$ , where  $l$  is the smallest value such that

$$307 \quad (3.7) \quad \frac{\sum_{i=1}^l \lambda_i}{\sum_{j=1}^{d_\mathbf{V}} \lambda_j} \geq \gamma, \quad 0 \leq \gamma \leq 1.$$

308  
 309 Finally, set

$$310 \quad (3.8) \quad \mathbf{V} = \mathbf{V} \mathbf{E}.$$

312 The parameters of the model fit to  $\mathbf{V}_1, \mathbf{V}_2, \dots, \mathbf{V}_N$  can be rescaled using Equations (3.5) and  
 313 (3.6).

314 **3.3. Conditional mean and covariance functions.** Given an estimate of the joint distri-  
 315 bution of  $\mathbf{V} = (\mathbf{W}', \mathbf{U}')'$  of the form in Equation (3.1), it is well known that the estimate of  
 316 the conditional mean function of  $\mathbf{W}$  given  $\mathbf{U} = \mathbf{u}_n$  for component  $k$  is,

$$317 \quad (3.9) \quad \hat{\boldsymbol{\mu}}_{\mathbf{W}|\mathbf{U}}^{(k)}(\mathbf{u}_n) = \hat{\boldsymbol{\mu}}_{\mathbf{W}}^{(k)} + \hat{\boldsymbol{\Sigma}}_{\mathbf{W}\mathbf{U}}^{(k)} \left( \hat{\boldsymbol{\Sigma}}_{\mathbf{U}\mathbf{U}}^{(k)} \right)^{-1} \left[ \mathbf{u}_n - \hat{\boldsymbol{\mu}}_{\mathbf{U}}^{(k)} \right],$$

318  
 319 where  $\hat{\boldsymbol{\Sigma}}_{\mathbf{V}}^{(k)}$  is the estimated covariance matrix for component  $k$ , which is partitioned according  
 320 to

$$321 \quad (3.10) \quad \hat{\boldsymbol{\Sigma}}_{\mathbf{V}}^{(k)} = \left[ \begin{array}{c|c} \hat{\boldsymbol{\Sigma}}_{\mathbf{W}\mathbf{W}}^{(k)} & \hat{\boldsymbol{\Sigma}}_{\mathbf{W}\mathbf{U}}^{(k)} \\ \hline \hat{\boldsymbol{\Sigma}}_{\mathbf{U}\mathbf{W}}^{(k)} & \hat{\boldsymbol{\Sigma}}_{\mathbf{U}\mathbf{U}}^{(k)} \end{array} \right].$$

322  
 323 The estimated conditional covariance matrix for component  $k$  is,

$$324 \quad (3.11) \quad \hat{\boldsymbol{\Sigma}}_{\mathbf{W}|\mathbf{U}}^{(k)}(\mathbf{u}_n) = \hat{\boldsymbol{\Sigma}}_{\mathbf{W}\mathbf{W}}^{(k)} - \hat{\boldsymbol{\Sigma}}_{\mathbf{W}\mathbf{U}}^{(k)} \left( \hat{\boldsymbol{\Sigma}}_{\mathbf{U}\mathbf{U}}^{(k)} \right)^{-1} \hat{\boldsymbol{\Sigma}}_{\mathbf{U}\mathbf{W}}^{(k)}.$$

325  
 326 If desired, summing over components gives the marginal moments,

$$327 \quad (3.12) \quad \hat{\boldsymbol{\mu}}_{\mathbf{W}|\mathbf{U}}(\mathbf{u}_n) = \sum_{k=1}^{\hat{K}} \hat{\boldsymbol{\mu}}_{\mathbf{W}|\mathbf{U}}^{(k)}(\mathbf{u}_n) \hat{\pi}_{k|\mathbf{u}_n},$$

328

329 and

$$330 \quad \hat{\boldsymbol{\Sigma}}_{\mathbf{W}|\mathbf{U}}(\mathbf{u}_n) = \sum_{k=1}^{\hat{K}} \hat{\boldsymbol{\Sigma}}_{\mathbf{W}|\mathbf{U}}^{(k)}(\mathbf{u}_n) \hat{\pi}_{k|\mathbf{u}_n} +$$

$$331 \quad (3.13) \quad \sum_{k=1}^{\hat{K}} \left( \hat{\boldsymbol{\mu}}_{\mathbf{W}|\mathbf{U}}^{(k)}(\mathbf{u}_n) - \hat{\boldsymbol{\mu}}_{\mathbf{W}|\mathbf{U}}(\mathbf{u}_n) \right) \left( \hat{\boldsymbol{\mu}}_{\mathbf{W}|\mathbf{U}}^{(k)}(\mathbf{u}_n) - \hat{\boldsymbol{\mu}}_{\mathbf{W}|\mathbf{U}}(\mathbf{u}_n) \right)' \hat{\pi}_{k|\mathbf{u}_n},$$

332

333 where

$$334 \quad (3.14) \quad \hat{\pi}_{k|\mathbf{u}_n} = \frac{\hat{\pi}_k \phi(\mathbf{u}_n; \hat{\boldsymbol{\mu}}_{\mathbf{U}}^{(k)}(\mathbf{u}_n), \hat{\boldsymbol{\Sigma}}_{\mathbf{U}\mathbf{U}}^{(k)})}{\sum_{l=1}^{\hat{K}} \hat{\pi}_l \phi(\mathbf{u}_n; \hat{\boldsymbol{\mu}}_{\mathbf{U}}^{(l)}(\mathbf{u}_n), \hat{\boldsymbol{\Sigma}}_{\mathbf{U}\mathbf{U}}^{(l)})}.$$

335  
336 Equations (3.12) and (3.13) follow from the law of iterated conditional expect-  
337 ation (e.g., [41], Equations (2b.3.4) and (2b.3.6)).

338 **3.4. Conditional distribution of the true state given a retrieved state.** The conditional  
339 distribution for a new draw from the distribution of  $\mathbf{U}$ , call it  $\mathbf{U}^*$  with realization  $\mathbf{u}^*$ , is

$$340 \quad (3.15) \quad \mathbf{W}^* \sim \text{GMM} \left( \hat{K}, \left\{ \hat{\boldsymbol{\mu}}_{\mathbf{W}|\mathbf{U}}^{(k)}(\mathbf{u}^*), \hat{\boldsymbol{\Sigma}}_{\mathbf{W}|\mathbf{U}}^{(k)}(\mathbf{u}^*), \hat{\pi}_{k|\mathbf{u}^*} \right\}_{k=1}^{\hat{K}} \right).$$

341  
342 One can explore this distribution by simulating from it, and summarize it (approximately) by  
343 calculating any desired summary quantities from the ensemble of simulated realizations.

344 **3.5. A simple example.** To illustrate the main aspects of our procedure, we appeal to a  
345 simple, low-dimensional example shown in Figure 3. The left panel shows a scatterplot of two  
346 (scalar) variables that exhibit a relationship (Equation (3.16)) that could be representative of  
347 a realistic, worst-case scenario. Not only is it non-linear, but the variances are heteroskedastic.

$$348 \quad (3.16) \quad W \sim N(5, 1), \quad U = (1.75)^W + \epsilon, \quad \epsilon \sim N(1, 2).$$

349  
350 There are a total of  $M = 5000$  ( $u_m, w_m$ ), pairs in the plot. The top-left panel shows the  
351 *forward relationship* between the two variables, with  $w$  analogous to realizations of  $\mathbf{W}$ , and  $u$   
352 analogous to realizations of  $\mathbf{U}$  in the subsections above. The top-right panel shows the inverse  
353 problem in which the goal is to infer  $w$  from noisy and potentially biased  $u$ . The bottom-right  
354 panel shows the estimated joint distribution of  $u$  and  $w$  fitted to these data using mclust.  
355 The values of both variables are standardized prior to fitting the model, and  $w$  is transformed  
356 back to its original scale. The joint distribution is a six-component Gaussian mixture, shown  
357 superimposed on the scatterplot, as six sets of Gaussian contours (the .68 and .95 contours).  
358 The corresponding component-specific regression lines for predicting  $w$  from  $u$  are shown in  
359 the bottom-right panel. For the  $k$ -th mixture component, the conditional mean, variance, and  
360 component membership probabilities of  $W$  given  $U = u$  are scalar versions of Equations (3.9),  
361 (3.11), and (3.14).

362 Now suppose a new value of  $U = u^*$ , is acquired and we wish to obtain the conditional  
363 distribution of  $W$  given  $U = u^*$ . Equipped with Equations (3.9) through (3.14), we first  
364 simulate  $B = 1000$  (say) *iid* draws from the discrete distribution that places probability  
365  $\pi_{k|u^*}$  on the indices  $k = 1, 2, 3, 4, 5, 6$ , and encode these outcomes in the random vector  $\boldsymbol{\kappa} =$   
366  $(\kappa_1, \kappa_2, \dots, \kappa_B)'$  of length  $B$ . Then, for each element of  $\boldsymbol{\kappa}$  we draw a random realization,  $w_b^*$ ,  
367 from the  $N(\mu^{(\kappa_b)}(u^*), \sigma^{(\kappa_b)}(u^*))$ , where  $\mu$  is the scalar version of  $\boldsymbol{\mu}$ , and  $\sigma$  is the scalar version  
368 of  $\boldsymbol{\Sigma}$ . The histogram of  $w_b^*$ ,  $b = 1, 2, \dots, B$  is an approximation of the conditional distribution  
369 of  $W$  given  $U = u^*$ . Figure 4 shows the simulated conditional distributions for two values  
370 of  $u^*$ , 13.76 and 22.41. Visual inspection suggests that the conditional standard deviations  
371 should decrease as one moves towards higher values of  $u^*$ , which they do.

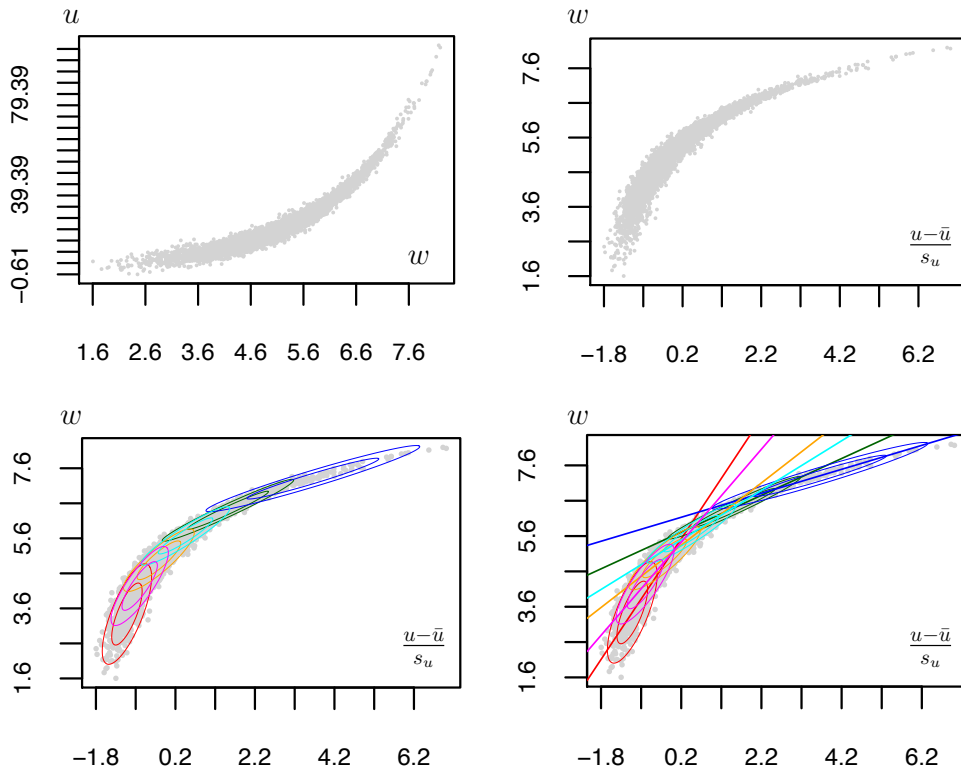


**Figure 3.** Simple example of fitting a GMM to an empirical ensemble,  $\{u_m, w_m\}_{m=1}^{5000}$ . Top-left: scatterplot of  $u$  on  $w$  showing the forward relationship. Top-right: scatterplot of  $w$  on  $u$  showing the inverse relationship. Bottom-left: Six-component GMM fitted to the joint distribution of  $u$  and  $w$ . Two density contours capturing 68 and 95 percent of the central mass of the Gaussian components are shown. Bottom-right: component-wise regression lines for the model. Component-wise variance is the vertical dispersion around the regression line at a fixed point on the  $x$ -axis. In the latter three plots, the  $u$  values have been standardized by subtracting the sample mean,  $\bar{u}$  and dividing by the sample standard deviation,  $s_u$ .

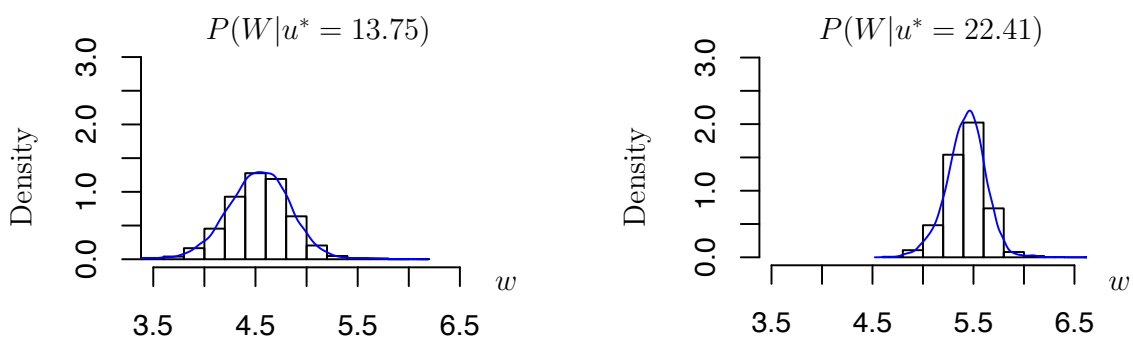


**Figure 4.** Simulated conditional densities of  $W$  given  $U^* = 13.76$  (left panel) and  $U^* = 22.41$  (right panel).  $w^*$  is on the standardized scale.

372 Figure 5 displays results of a cross-validation experiment that compares nominal and actual  
 373 coverage probabilities for 50 percent and 95 percent confidence intervals. In this experiment,  
 374 we use the same 5000  $(u, w)$  pairs shown in the center panel of Figure 3. We randomly divide  
 375 these into a training set of 2500  $(u, w)$  pairs, and a test set of 2500  $(u^*, w^*)$  pairs. We fit a  
 376 GMM to the training set, plug each value of  $u^*$  in the test set into the Equations (3.9) through  
 377 (3.14), and simulate 1000 draws from the posterior distributions of  $W^*$  given  $U^*$ . Finally, we  
 378 compute the 0.025, 0.250, 0.750, and 0.975 quantiles of each of these empirical conditional  
 379 distributions ( $Q_{.025}$ ,  $Q_{.25}$ ,  $Q_{.75}$ , and  $Q_{.975}$ ) and determine what proportion of the 2500 test  
 380 set pairs have the property that  $w^*$  lies inside the 95 percent interval defined by  $[Q_{.025}, Q_{.975}]$ ,  
 381 and similarly, inside the 50 percent interval defined by  $[Q_{.25}, Q_{.75}]$ .

$$382 \quad p_{.95,1} = \frac{1}{2500} \sum_{i=1}^{2500} 1 [Q_{.025} \leq w_i^* \leq Q_{.975}],$$

$$383 \quad (3.17) \quad p_{.50,1} = \frac{1}{2500} \sum_{i=1}^{2500} 1 [Q_{.25} \leq w_i^* \leq Q_{.75}].$$

385 We carry out this entire simulation procedure 200 times to obtain  $p_{.95,b}$  and  $p_{.50,b}$ , for  $b =$   
 386  $1, 2, \dots, B = 200$ . Figure 5 shows that the actual coverage probabilities are always, or nearly  
 always, consistent with the nominal coverage probabilities.

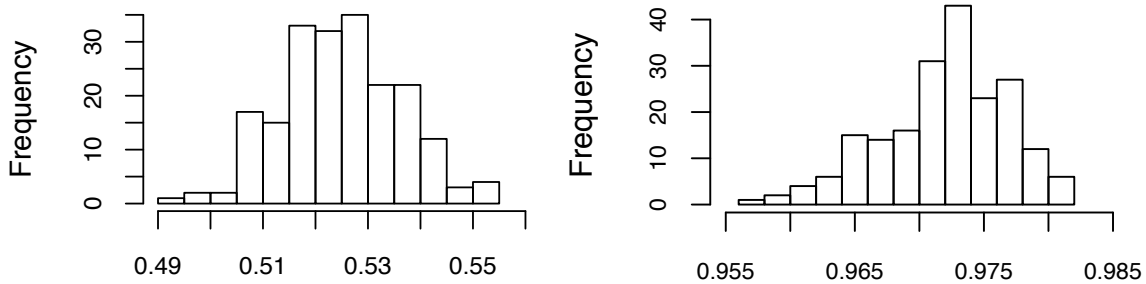


Figure 5. Histograms of actual proportions of test set values of  $w$  contained within the central 50 percent (left) and 95 percent (right) of the estimated conditional distribution of  $W$  given  $U$ , over 200 trials of the simulation experiment. In each trail, a randomly selected half of the  $(u, w)$  pairs in Figure 3 were assigned to the training set, and other other half to the test set.

387

388

389

390

391

392

393

394

395

396

397

In the next section we describe in detail how we implement our approach for our motivating application, the Orbiting Carbon Observatory-2 mission. It is considerably more complex than the simple example just presented, but nonetheless analogous in many respects. The main difference is that the predictor is high-dimensional, although the predictand remains a scalar. Other differences include the fact that we did not need to deal with model discrepancy in the simple example, but we do for OCO-2; and perhaps most importantly, how we set up the simulation experiment that allows us to learn the mechanistic properties of the retrieval estimator.

396

397

**4. Application to OCO-2.** NASA's OCO-2 instrument was launched into Earth orbit on July 2, 2014. Its primary scientific objective is to estimate total column concentrations

398 (dry air mole-fractions) of carbon dioxide for use in estimating carbon fluxes between Earth’s  
 399 surface and atmosphere. Details of the OCO-2 mission and its retrievals can be found in  
 400 [2, 14, 9, 13, 6]. OCO-2, along with Japan’s GOSAT [44, 57] and GOSAT-2 missions, China’s  
 401 TanSAT [56], and OCO-3 [15] now form a fleet of observing systems that all use similar  
 402 technology, including optimal estimation for retrievals. What we describe below for OCO-2 is  
 403 also applicable to these and other missions potentially observing other variables, with suitable  
 404 modifications.

405 The primary OCO-2 QOI is total column mole-fraction of CO<sub>2</sub>, called XCO<sub>2</sub>. It is the  
 406 number of molecules of carbon dioxide divided by the number of molecules of dry air (total air  
 407 molecules minus water molecules), in a vertical column of the atmosphere. This quantity is  
 408 derived on a sounding-by-sounding basis for cloud-free, trapezoidal ground footprints measur-  
 409 ing 2.25 km along-track and 1.29 km across-track during the spacecraft’s south-to-north polar  
 410 orbit. The OCO-2 state vector,  $\mathbf{X}$ , includes a 20-element vertical profile of estimated CO<sub>2</sub>  
 411 mole-fractions at various altitudes, as well as quantities describing aerosol, cloud, and surface  
 412 properties. XCO<sub>2</sub> is a scalar quantity computed by multiplying the CO<sub>2</sub> profile,  $\mathbf{X}_{1:20}$ , by a  
 413 location-specific pressure weighting function,  $\mathbf{h}$ ,

$$414 \quad (4.1) \quad \mathbf{X} = \mathbf{h}' \mathbf{X}_{1:20}.$$

415 In the next subsection, we provide details of how we applied our methodology described in  
 416 Section 3 specifically for the OCO-2 case.

418 **4.1. Post hoc uncertainty quantification.** We applied our method to a set of retrievals  
 419 from the OCO-2 Version 7 data product [13] for week-long periods over four months spanning  
 420 the four seasons: August and November 2015 and February and May 2016. Here, we report  
 421 results for retrievals that are coincident in time and space with ground-based measurements  
 422 that are considered, for practical purposes, ground truth.

423 Figure 6 is a modified version of Figure 2 that shows our implementation for OCO-2. The  
 424 main steps are described in the following sub-sections. Green section numbers in parentheses  
 425 in the figure direct the reader to relevant sections of the text.

426 **4.1.1. Generating synthetic true state ensembles.** In Figure 6, the single marginal dis-  
 427 tribution in Figure 2 is replaced by a set of distributions,  $\tilde{P}_r$ ,  $r = L1, \dots, L11$ . The index  $r$   
 428 refers to sub-regions of the globe we call templates. Figure 7 shows the geographic domains of  
 429 41 such regions defined by colleagues in the user community who specialize in flux inversion.  
 430 We asked these domain experts to define areas over which we could expect the behavior of  
 431 OCO-2 state vectors, over a single calendar week, to be representative of specific underlying  
 432 physical processes generating them. This allows us to invoke the standard assumption of er-  
 433 godicity in time and space. We carried out these simulations for all land and ocean regions  
 434 with sufficient OCO-2 data. However, here we present results for land regions only because  
 435 this is where corroborating ground-based information is available.

436 Next, we fitted multivariate Gaussian mixture models to collections of actual, retrieved  
 437 OCO-2 state vectors belonging to the templates, and in a single calendar week. We sampled  
 438 5000 times from each of these distributions to generate template-week-specific ensembles of  
 439 synthetic true states. Sampling from the fitted distributions is a semi-parametric analog to  
 440 bootstrap resampling typically used in the bootstrap bias correction. Finally, we combined

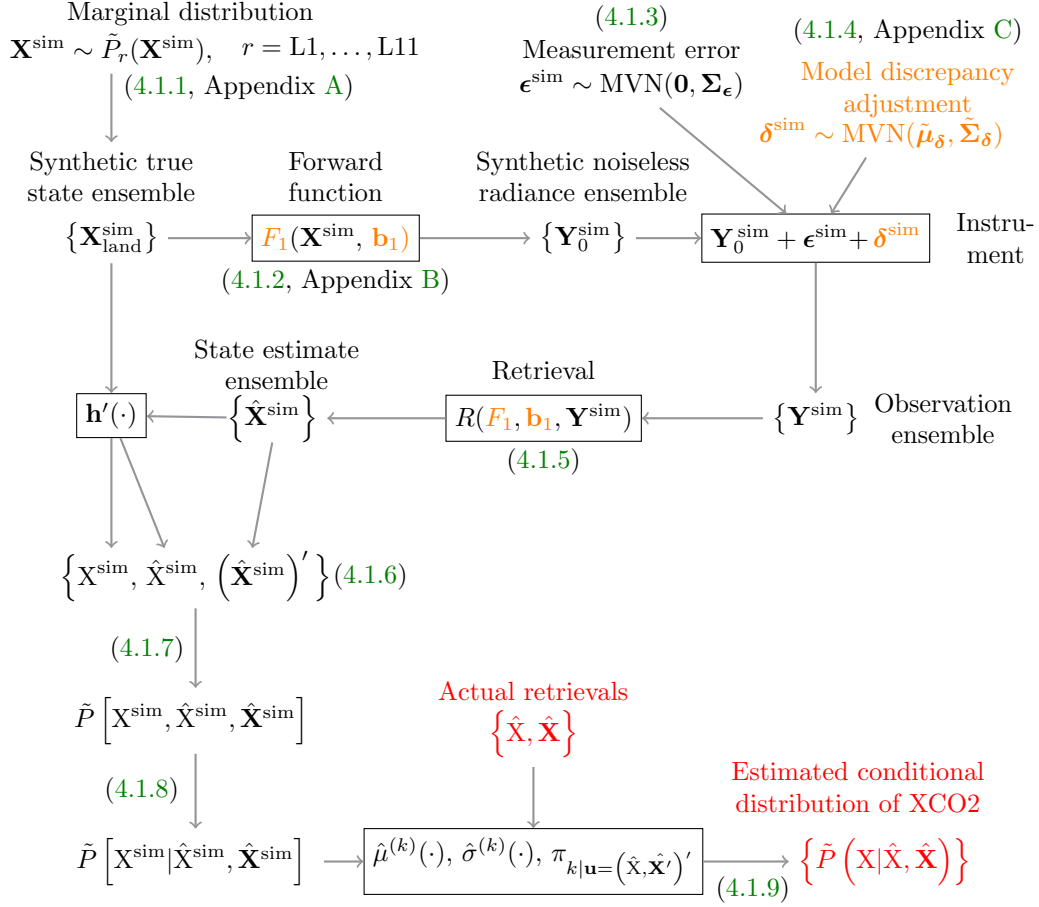


**Figure 6.** Conceptual diagram of the uncertainty quantification strategy for OCO-2’s OE retrieval. Green numbers in parentheses indicate subsections containing detailed explanations.

441 the eleven synthetically created ensembles to form the synthetic true state ensemble,  $\{\mathbf{X}^{\text{sim}}\}$ ,  
 442 for the week being processed:

$$443 \quad (4.2) \quad \mathbf{X}_{\text{land}}^{\text{sim}} \equiv \begin{pmatrix} \mathbf{X}_{L1}^{\text{sim}} \\ \vdots \\ \mathbf{X}_{L11}^{\text{sim}} \end{pmatrix}.$$

444

445 Appendix A provides additional details of model fitting and resampling. The stacked matrices  
 446 in Equation (4.2) are abbreviated by  $\{\mathbf{X}^{\text{sim}}\}$  in Figure 6.

447 **4.1.2. The forward function and its parameters.** We applied the OCO-2 forward *model*,  
 448  $F_1$ , to each simulated true state vector in  $\mathbf{X}_{\text{land}}^{\text{sim}}$ .  $F_1$  is the same forward model used opera-  
 449 tionally by OCO-2 in Version 7 of its Atmospheric Carbon Observations from Space (ACOS)  
 450 retrieval algorithm [13, 34]. The ACOS forward model is often termed “full-physics” (FP).  
 451 Further details are provided in Appendix B and [2].

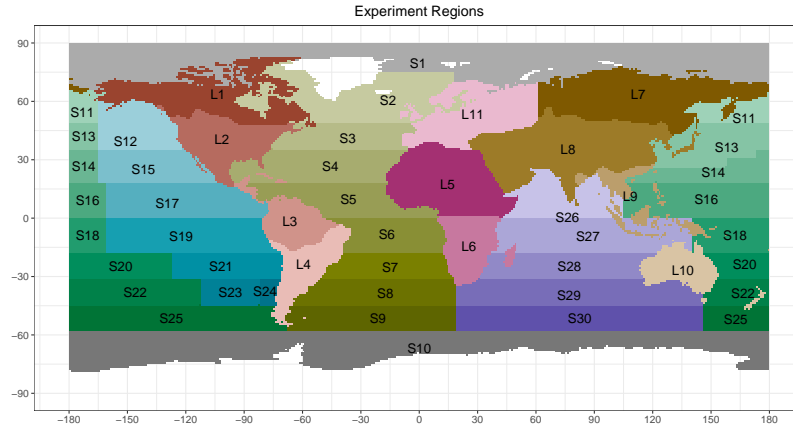


**Figure 7.** Forty-one regions defining the spatial partitioning of OCO-2 data for template definition. There are 30 ocean regions with labels prefixed by “S”, and 11 land regions with labels prefixed by “L”.

452 **4.1.3. Measurement error.** The simulation of the measurement error,

$$453 \quad \epsilon^{\text{sim}} \sim \text{MVN}(\mathbf{0}, \Sigma_{\epsilon}),$$

455 follows the OCO-2 instrument noise specification [14]. The noise covariance matrix  $\Sigma_{\epsilon}$  is  
456 diagonal with elements

$$457 \quad (4.3) \quad \sigma_{\epsilon,i}^2 = \text{var}(\epsilon_i^{\text{sim}}) = b_{\epsilon,1,i} Y_{0,i}^{\text{sim}} + b_{\epsilon,2,i},$$

459 where the  $b_{\epsilon,1,i}$  and  $b_{\epsilon,2,i}$  are instrument calibration parameters, and  $i$  indexes elements in the  
460 radiance vector. This model suggests the noise variance is proportional to the mean signal,  
461 with an additive offset.

462 **4.1.4. Model discrepancy adjustment.** In Figure 6 we used the same forward model  
463 and forward model parameters to produce both simulated radiances and to retrieve the state  
464 estimate from them (see Subsection 4.1.2). This is overly optimistic since it implies that the  
465 retrieval’s forward model is a perfect representation of nature’s true forward function. On the  
466 other hand, the true forward function  $F_0(\cdot, \mathbf{b}_0)$  is not known, and the best available forward  
467 model is  $F_1(\cdot, \mathbf{b}_1)$ . To compensate for this, we added an additional component of random  
468 error to the radiance vectors which we believe realistically degrades the radiances to account  
469 for using  $F_1(\cdot, \mathbf{b}_1)$  where we should have used  $F_0(\cdot, \mathbf{b}_0)$ . We degraded the radiance vector by  
470 adding this “model discrepancy” adjustment,  $\delta^{\text{sim}}$ , at the same time we added  $\epsilon$  to mimic  
471 measurement error of the instrument.

472 The model discrepancy adjustment is an  $(L_{\mathbf{Y}} \times 1)$ -dimensional perturbation modeled as  
473 a draw from a multivariate Gaussian distribution with mean  $\tilde{\boldsymbol{\mu}}_{\delta}$  and covariance matrix  $\tilde{\Sigma}_{\delta}$ .  
474 The Gaussian choice is for convenience, and may be revisited in the future. We estimated  
475 model parameters by comparing distributions of the *spectral residuals* in the simulation with  
476 those produced by the actual OCO-2 retrieval process. Spectral residuals are the differences  
477 between the observed OCO-2 radiance vectors and the radiance vectors predicted by applying

478 the OCO-2 forward model to the retrieved state vector estimate. Appendix C describes in  
479 detail how we estimate the parameters  $\tilde{\boldsymbol{\mu}}_\delta$  and  $\tilde{\boldsymbol{\Sigma}}_\delta$ .

480 **4.1.5. The retrieval.** The OCO-2 operational retrieval was performed for each  $\mathbf{Y}^{\text{sim}}$ . The  
481 retrieval’s assumed statistical parameters  $\mathbf{b}_1$ , including the prior mean vector and covariance  
482 matrix used in OE, were set to the operational values present at a reference sounding at  
483 the geographical center of the template to which  $\mathbf{Y}^{\text{sim}}$  belonged. The operational retrieval  
484 performs a numerical search for the minimum of an objective function that includes the  
485 Gaussian negative log-likelihood of the radiances and a regularization term due to a Gaussian  
486 prior distribution specified as part of OE. This was implemented with a Levenberg-Marquardt  
487 algorithm with step sizes, relaxation, and convergence criteria defined for the operational  
488 retrieval [2]. The OCO-2 inverse problem is moderately non-linear [5], so these optimization  
489 parameters can impact the overall retrieval quality. We retained those retrievals  $\hat{\mathbf{X}}^{\text{sim}}$  that  
490 successfully converged within the allowed number of iterations, and discarded those that did  
491 not.

492 **4.1.6. Assembling the empirical joint distribution.** We used the set of synthetic true  
493 states and their corresponding synthetic retrieved state vectors to form an empirical sample  
494 of the joint distribution of the two. The QOIs were XCO2 values,  $X^{\text{sim}}$ , created from the  
495 synthetic true state vectors using Equation (4.1). The predictors were the corresponding  
496 synthetic retrieved state vectors,  $\hat{\mathbf{X}}^{\text{sim}}$ , with retrieved XCO2 derived from them:  $\hat{X}^{\text{sim}} =$   
497  $\mathbf{h}'\mathbf{X}_{1:20}^{\text{sim}}$ , appended. The training ensembles used to estimate the GMM parameters for the  
498 resampling step were,

$$499 \quad (4.4) \quad \left\{ X_m^{\text{sim}}, \hat{X}_m^{\text{sim}}, \left( \hat{\mathbf{X}}_m^{\text{sim}} \right)' \right\}_{m=1}^{M_{\text{land}}},$$

501 where  $M_{\text{land}} = \sum_{r=L1}^{L11} M_r$ , and  $M_r$  was the number of successful simulated retrieved state  
502 vectors in template  $r$ . It may seem that including  $\hat{X}_m^{\text{sim}}$  as a predictor duplicates the infor-  
503 mation already in  $\hat{\mathbf{X}}_m^{\text{sim}}$ . It does not:  $\hat{X}_m^{\text{sim}}$  includes the pressure weighting function. Offline  
504 experiments strongly suggested that predictions of  $X_m^{\text{sim}}$  improve substantially when  $\hat{X}_m^{\text{sim}}$  is  
505 included as a predictor.

506 We made one further modification to the training ensembles before estimating the joint  
507 distributions of predictors and predictands: six elements of the state vector were removed  
508 because they were found to degrade the predictions of  $X^{\text{sim}}$ . The deleted elements were coef-  
509 ficients describing the distributions of cloud ice and liquid water in the atmospheric column.

510 **4.1.7. Fitting the Gaussian mixture model.** To estimate the joint distribution of XCO2  
511 and the predictors from the empirical ensembles in Equation (4.4), we followed the method-  
512 ology described in Section 3.2, with

$$513 \quad (4.5) \quad \mathbf{V} = \left( X^{\text{sim}}, \hat{X}^{\text{sim}}, \left( \hat{\mathbf{X}}^{\text{sim}} \right)' \right)'$$

515 To increase speed in the density estimation step, we reduced the dimension of  $\mathbf{V}$  by converting  
516 the variables that will play the role of predictors to their corresponding values in the space of

517 their leading principal components. To be clear, we partitioned  $\mathbf{V} = (\mathbf{W}, \mathbf{U})'$  where

$$518 \quad (4.6) \quad \mathbf{W} = \mathbf{X}^{\text{sim}}, \quad \text{and} \quad \mathbf{U} = \left( \hat{\mathbf{X}}^{\text{sim}}, \left( \hat{\mathbf{X}}^{\text{sim}} \right)' \right)'. \\ 519$$

520 In determining leading eigenvectors, we used the threshold  $\gamma = 0.99$  here. (See Equation (3.7).)  
 521 We used *densityMclust* function (in the R package *mclust*) to fit a family of Gaussian mixture  
 522 models. The software requires us to specify the maximum number of allowable components,  
 523 and it uses the Bayesian Information Criterion to select the best model. We set the maximum  
 524 to 20 on the grounds 1) the number should exceed the number used for estimating GMM's  
 525 for individual template-weeks in the resampling stage (see Appendix A), and 2) the number  
 526 should be small enough to be interpretable and to achieve moderate computational speed.

527 The last step was to use the datum-specific weights in Equation (3.3) to convert the model's  
 528 estimated parameters back to the original scale of the data via the formulas in Equation  
 529 (3.6). The values of the parameters  $\hat{K}^{\text{sim}}$  and  $\hat{\pi}_1^{\text{sim}}, \hat{\pi}_2^{\text{sim}}, \dots, \hat{\pi}_{\hat{K}^{\text{sim}}}^{\text{sim}}$  remained unchanged. The  
 530 estimated mixture density for land in a given calendar week is,

$$531 \quad (4.7) \quad \left( \mathbf{X}^{\text{sim}}, \hat{\mathbf{X}}^{\text{sim}}, \left( \hat{\mathbf{X}}^{\text{sim}} \right)' \right)' = (\mathbf{W}, \mathbf{U})' \sim \text{GMM} \left( \hat{K}^{\text{sim}}, \left\{ \hat{\boldsymbol{\mu}}_k^{\text{sim}}, \hat{\boldsymbol{\Sigma}}_k^{\text{sim}}, \hat{\pi}_k^{\text{sim}} \right\}_{k=1}^{\hat{K}^{\text{sim}}} \right), \\ 532$$

533 where

$$534 \quad (4.8) \quad \hat{\boldsymbol{\mu}}_k^{\text{sim}} = \left( \hat{\boldsymbol{\mu}}_{k\mathbf{W}}^{\text{sim}}, \left( \hat{\boldsymbol{\mu}}_{k\mathbf{U}}^{\text{sim}} \right)' \right)', \quad \text{and} \quad \hat{\boldsymbol{\Sigma}}_k^{\text{sim}} = \begin{pmatrix} \hat{\sigma}_{k\mathbf{W}\mathbf{W}}^{\text{sim}} & \hat{\boldsymbol{\Sigma}}_{k\mathbf{W}\mathbf{U}}^{\text{sim}} \\ \hat{\boldsymbol{\Sigma}}_{k\mathbf{U}\mathbf{W}}^{\text{sim}} & \hat{\boldsymbol{\Sigma}}_{k\mathbf{U}\mathbf{U}}^{\text{sim}} \end{pmatrix}, \\ 535 \\ 536$$

537 **4.1.8. Estimating the conditional distribution of XCO2 given retrieval predictors.** We  
 538 use Equations (3.9) through (3.14) to compute the Gaussian components' conditional means  
 539 and variances of XCO2, given actual OCO-2 retrievals,  $\mathbf{u}^* = (\hat{\mathbf{X}}, \hat{\mathbf{X}}')$ . Thus, for each actual  
 540 OCO-2 sounding,  $\mathbf{u}^*$ , we have the conditional distribution,

$$541 \quad (4.9) \quad \mathbf{W}^* \sim \text{GMM} \left( \hat{K}^{\text{sim}}, \left\{ \hat{\boldsymbol{\mu}}_{\mathbf{W}|\mathbf{U}}^{(k)}(\mathbf{u}^*), \hat{\sigma}_{\mathbf{W}|\mathbf{U}}^{(k)}(\mathbf{u}^*), \hat{\pi}_{k|\mathbf{u}^*} \right\}_{k=1}^{\hat{K}^{\text{sim}}} \right). \\ 542$$

543 **4.1.9. Simulating from sounding-specific conditional distributions of XCO2.** These dis-  
 544 tributions can be approximated by simulating from Equation (4.9), and summary statistics  
 545 can be computed as needed. To simulate  $B$  realizations,  $\mathbf{W}_b^*$ , for  $b = 1, \dots, B$ , from the model  
 546 in Equation (4.9):

547 1. Let  $\kappa_b$  be a univariate random variable taking values in the set  $\{1, \dots, \hat{K}^{\text{sim}}\}$  with,

$$548 \quad P(\kappa_b = k) = \hat{\pi}_{k|\mathbf{u}^*}, \quad k \in \{1, \dots, \hat{K}^{\text{sim}}\}. \\ 549$$

550 2. Draw  $B$  random variables,

$$551 \quad \mathbf{W}_b^* \sim N \left( \hat{\boldsymbol{\mu}}_{\mathbf{W}|\mathbf{U}}^{(\kappa_b)}(\mathbf{u}^*), \hat{\sigma}_{\mathbf{W}|\mathbf{U}}^{(\kappa_b)}(\mathbf{u}^*) \right), \quad b = 1, \dots, B. \\ 552$$

553 If desired, the marginal mean and variance functions can be obtained by integrating over the  
 554 mixture components as in Equations (3.12) and (3.13).

555 **4.2. Comparison to ground station data.** In this subsection we evaluate how well our  
 556 method performs by comparing ground station observations of total column CO<sub>2</sub> at locations  
 557 where they exist, to our simulated conditional distributions and to distributions implied by  
 558 the OCO-2 operational retrieval output. We utilized ground-based CO<sub>2</sub> data collected by  
 559 the Total Carbon Column Observing Network (TCCON) [54] and coincident retrievals from  
 560 OCO-2. TCCON data are used to validate OCO-2 XCO<sub>2</sub> point estimates delivered by the  
 561 mission [55]. That validation procedure also involves comparing XCO<sub>2</sub> estimates to TCCON,  
 562 among other things, but it does not include any analysis of the operationally-derived variance  
 563 or the accuracy of the Gaussian assumption.

564 We quantified performance of conditional distribution estimates with two simple metrics.  
 565 The first is the position of the observed TCCON value within the conditional distribution,

$$566 \quad G_{op}(X_T) = P_{op}(X \leq X_T) \approx \Phi(X_T; \hat{X}, \hat{S}),$$

$$567 \quad (4.10) \quad G_s(X_T) = P_s(X \leq X_T) \approx \frac{1}{B} \sum_{b=1}^B \mathcal{I}(W_b^* \leq X_T),$$
 568

569 where *op* and *s* denote operational and simulated conditional distributions, respectively. The  
 570 scalar quantity  $\hat{S}$  is the conditional variance of XCO<sub>2</sub> given the observed radiance, as estimated  
 571 by the retrieval algorithm through a linear approximation [2].  $X_T$  is the TCCON value,  
 572  $\Phi(x; \mu, \sigma^2)$  is the value of the Gaussian cumulative distribution function with mean  $\mu$  and  
 573 variance  $\sigma^2$  evaluated at  $x$ . The variable  $B$  is the number of draws from the simulated  
 574 distribution used to approximate it, and  $W_b^*$  is the  $b$ -th draw. Finally,  $\mathcal{I}(\cdot)$  is the indicator  
 575 function taking value one if its argument is true and zero otherwise. Good performance is  
 576 achieved when the TCCON value is centrally located, and poor performance is indicated by a  
 577 TCCON value far out in a tail. So values of  $G_{op}(X_T)$  and  $G_s(X_T)$  near 0.5 are judged superior  
 578 to those that are close to zero or one.

579 The second metric is the bias of the conditional mean relative to the TCCON value:

$$580 \quad (4.11) \quad \beta_{op}(X_T) = (\hat{X} - X_T) \quad \text{and} \quad \beta_s(X_T) = \left( \frac{1}{B} \sum_{b=1}^B W_b^* \right) - X_T.$$
 581

582 This is important because the primary use of OCO-2 XCO<sub>2</sub> estimates is as input into flux  
 583 inversion models. These models *assume* that XCO<sub>2</sub> estimates are unbiased. If bias does  
 584 nonetheless exist, it can lead to spurious flux estimates, particularly if there are systematic  
 585 spatial patterns.

586 To ensure direct comparability, we limited our analysis to OCO-2 soundings with ge-  
 587 ographic centers in very small regions of size 0.01° in both latitude and longitude around  
 588 TCCON locations. One degree of longitude is approximately 100 kilometers at the Equator,  
 589 and less as one moves north or south. Since OCO-2 footprints span 1.29 kilometers of longitude

590 and 2.25 kilometers of latitude, this restriction limited the soundings we used to those that  
591 contain the TCCON site. To identify a single TCCON value to serve as a benchmark, we used  
592 the value for which the time of acquisition was between the earliest and latest sounding times,  
593 among those soundings satisfying the  $0.01^\circ$  spatial proximity criterion. In some weeks at some  
594 TCCON sites, there were no data available either because there was no TCCON observation  
595 within the very brief overpass time window, or because there were no successful retrievals  
596 within the spatial overlap region. There was never more than one TCCON benchmark value.

597 For illustration, consider four soundings' conditional distributions shown in Figure 8.  
598 These four are representative of the types of relationships between operational and simulation-  
599 based conditional distributions observed in our analysis. In the figure, the top two panels are  
600 soundings covering the Lamont, OK TCCON site during the week of November 2, 2015, and  
601 the bottom two panels cover the TCCON site at Tsukuba, Japan during the week of May  
602 13, 2016. There are a total 132 and 77 soundings that satisfy the  $0.01^\circ$  spatial criterion,  
603 respectively. In all panels, the red curves are the simulation-based conditional distributions'  
604 approximations based  $B = 100,000$  realizations of  $W_b^*$ , and the blue curves are Gaussian dis-  
605 tributions with means and variances equal to the operationally retrieved moment estimates.  
606 The green vertical lines are the TCCON values. In both Lamont results (top row), the bias of  
607 the simulation-based estimate is smaller than that of the operational estimate. The left panel  
608 shows a case in which  $X_T$  is more consistent (in the sense of being more centrally located) with  
609 the simulation-based distribution than with the operationally derived. For Tsukuba (bottom  
610 row), the absolute value of the bias is actually lower for the operational estimate, and the  
611 biases are of different signs. The TCCON value is much more consistent with the simulation-  
612 based distribution than with the operational distribution in the left panel, but the TCCON  
613 value is consistent with neither distribution in the right panel.

614 In Figure 9 we summarize comparisons like those in Figure 8, for all 944 soundings  
615 used in our analysis. The horizontal axis reflects the difference between the operational  
616 and simulation-based conditional distributions with respect to the centrality of the TCCON  
617 value in those distributions. The vertical axis is the difference between the absolute biases  
618 of the means of the two distributions, relative to TCCON. Points in the lower-left quadrant  
619 (colored blue) represent those soundings for which the simulation-based method is superior in  
620 both metrics. These comprise 63.1 percent of soundings used in this analysis. Points in the  
621 upper-left quadrant (colored green) represent those footprints for which the simulation-based  
622 method is superior with respect to the cumulative distribution function metric, but inferior  
623 with respect to the bias metric. These comprise 25.7 percent of soundings. For most of these,  
624 the difference in absolute bias is less than 1.25 parts per million. 11.2 percent of the footprints  
625 fall in the upper-right quadrant (colored red). In these cases the operational distribution is  
626 superior to the simulation-based distribution on both metrics. An example of such a case  
627 would be where the operational retrieval does very well, having mean very near the TCCON  
628 value and a low reported variance, while the simulation-based distribution has a long right (or  
629 left) tail. This will pull the mean of the simulation-based distribution away from the TCCON  
630 value, and cause the TCCON value to be less centrally located. However, given the tendency  
631 of operational variance estimates to be too low, such occurrences should be interpreted with  
632 caution.

633 As a final step in the evaluation of our methodology and comparison of it to that invoked

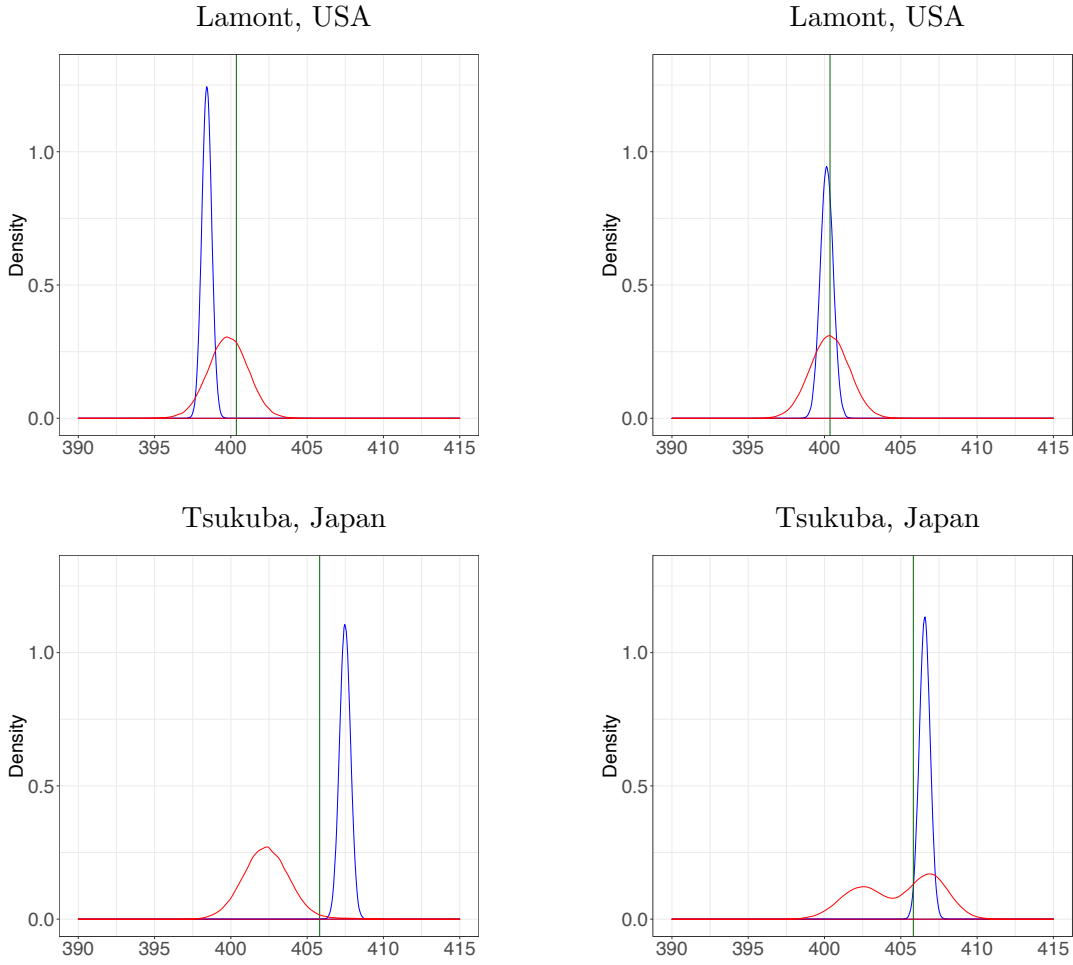


**Figure 8.** Comparisons of typical operational (blue) and simulation-based (red) posterior distributions, to TCCON values (green). Top-left and Top-right: Two soundings near Lamont, OK during the week of November 2, 2015. Bottom-left and bottom-right: Two soundings near Tsukuba, Japan during the week of May 13, 2016.

634 by the operational retrieval algorithm, we examine coverage probabilities. The conditional  
 635 distributions of soundings coincident in time and space with a TCCON site can be used to  
 636 derive an ensemble of confidence intervals for the corresponding TCCON value. Approximate  
 637  $(1 - \alpha)$  percent confidence intervals for TCCON XCO<sub>2</sub> derived from the simulated and  
 638 operationally-retrieved conditional distributions, respectively, are

$$639 \quad (4.12) \quad \left[ Q_{\alpha/2}^s, Q_{1-\alpha/2}^s \right] \quad \text{and} \quad \left[ Q_{\alpha/2}^{op}, Q_{1-\alpha/2}^{op} \right],$$

641 where  $Q_{\alpha/2}$  and  $Q_{1-\alpha/2}$  are the  $(\alpha/2)$  and  $(1 - (\alpha/2))$  empirical quantiles of the appropriate  
 642 distributions.

643 For a given TCCON site and calendar week, let  $N$  be the number of soundings that satisfy  
 644 the spatial proximity criterion of  $0.01^\circ$  and for which there exists a single TCCON estimate

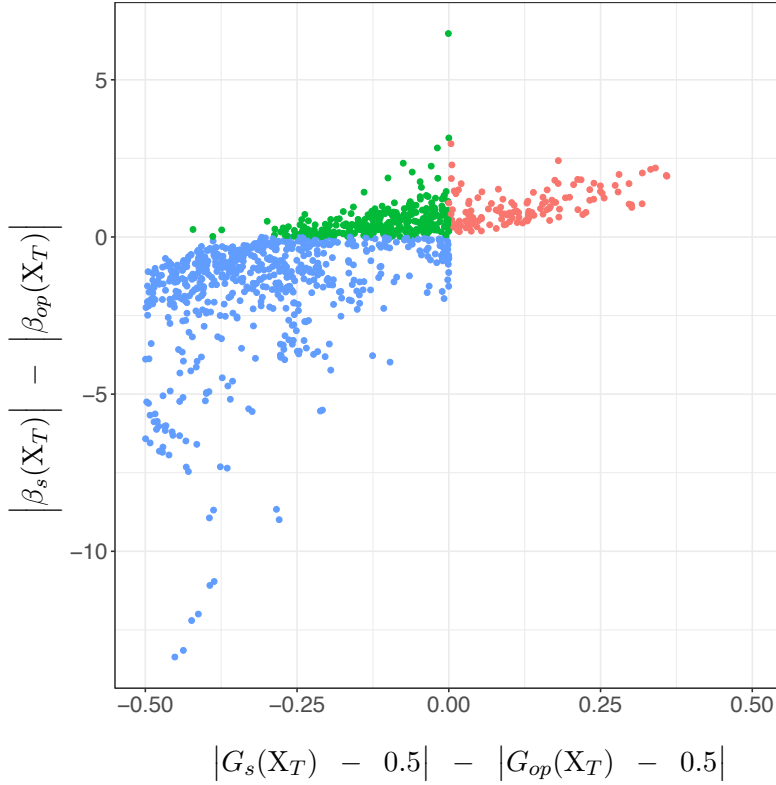


**Figure 9.** Comparisons of operational and simulation-based conditional distribution estimates using two metrics. The horizontal axis is the difference in how centrally located the TCCON observations is with respect to the two distributions. The vertical axis is the difference in the distributions' means (in ppm) relative to TCCON. Each point represents a sounding that overlaps a TCCON site. The points' colors correspond to the quadrant of the space in which they lie.

645 of  $X_{CO2}$ ,  $X_T$ . We computed,

$$646 \quad (4.13) \quad p_{1-\alpha}^s = \frac{1}{N} \sum_{n=1}^N \mathcal{I} \left( X_T \in \left[ Q_{\alpha/2}^s, Q_{1-\alpha/2}^s \right] \right), \text{ and}$$

$$647 \quad (4.14) \quad p_{1-\alpha}^{op} = \frac{1}{N} \sum_{n=1}^N \mathcal{I} \left( X_T \in \left[ Q_{\alpha/2}^{op}, Q_{1-\alpha/2}^{op} \right] \right),$$

648

649 for each site-week for  $\alpha = 0.05$  and  $\alpha = 0.50$ . Results are displayed in Table 1.

650 None of the empirical coverage probabilities derived from the operational distributions  
 651 agree with the nominal coverage. In contrast, the simulation-based coverages meet or exceed  
 652 the nominal values for five of the eight site-weeks. In addition, empirical coverage exceeds  
 653 the nominal value for  $p_{.50}^s$  at Orleans, and is close for Lauder at  $p_{.95}^s$ . Performance is poor for  
 654 Sodankyla, which is at high latitude, and is a notoriously difficult site for retrievals in general.  
 655 We plan further in-depth investigations to understand how different geographic conditions  
 656 influence performance of the simulation-based method.

Site	Week	$p_{.95}^{op}$	$p_{.50}^{op}$	$p_{.95}^s$	$p_{.50}^s$	$N$
Bialystok, Poland	2016-02-17	0.013	0.000	1.000	1.000	80
Darwin, Australia	2015-08-10	0.663	0.366	0.970	0.782	202
Lamont, OK USA	2015-11-02	0.288	0.143	1.000	0.909	132
Lauder, New Zealand	2016-02-29	0.449	0.170	0.932	0.441	118
Orleans, France	2015-11-02	0.627	0.322	0.746	0.661	59
Sodankyla, Finland	2015-08-20	0.533	0.133	0.600	0.267	15
Tsukuba, Japan	2016-05-13	0.390	0.169	0.974	0.818	77
Wollongong, Australia	2015-11-24	0.272	0.115	0.973	0.778	261

Table 1

Coverage probabilities over ensembles of confidence intervals derived from operational and simulation-based conditional distributions. Values in green indicate empirical coverages at least as large as nominal values.

657 **5. Summary and discussion.** The primary challenge addressed by this work is that of  
658 providing uncertainties for estimates of physical states produced by remote sensing retrieval  
659 algorithms. We define uncertainty as the conditional distribution of the true state given the  
660 estimated state; this is a probabilistic quantification of what remains unknown about the  
661 QOI after seeing the estimate. The methodology we propose approximates this conditional  
662 distribution for every sounding for which a retrieved state point estimate exists.

663 Our method is similar in spirit to the bootstrap bias correction in using the relationship  
664 between an original sample and a set of resamples taken from it, as a proxy for the relationship  
665 between the unknown truth, and the original sample itself. Here, we extend the idea beyond  
666 bias correction alone. We model the full conditional distribution of the true state given a  
667 corresponding retrieved state, as a weighted mixture of Gaussian regressions. Then, any  
668 operationally-retrieved state estimate can be used as a predictor.

669 There are a number of significant benefits of this approach. First, it does not require  
670 enumerating particular sources of uncertainty in order to be complete. The mixture regres-  
671 sion models capture what is known about the aggregated effects of all uncertainty sources,  
672 including “unknown unknowns” (e.g., higher-order interaction effects) in the operational pro-  
673 cessing chain. This is, of course, assuming that the resampling procedure produces repre-  
674 sentative ensembles of what the operational observing system encounters. Second, forward  
675 model structural and parametric uncertainties are approximated by the model discrepancy  
676 term. Identifying the role of spectral residuals in estimating model discrepancy opens the  
677 door to future experiments and empirical analyses that may help improve the forward model.  
678 Third, the entire approach is independent of how the retrieved state estimates are produced.  
679 Fourth, since we modeled the joint and conditional distributions as Gaussian mixtures, these  
680 distributions may have general non-Gaussian forms. Finally, the entire procedure is executed  
681 separately from the operational retrieval process, and can be performed without interfering  
682 with operations. Once the simulations are run and the model is fitted, the rest of the compu-  
683 tation is very fast and easily applied to the operational output.

684 Looking to the future, we are exploring spatial and spatio-temporal extensions to our  
685 method. Instead of simulating ensembles of independent and identically distributed synthetic  
686 true states, we simulate entire spatial fields (e.g., [26]) at once. We are now applying that idea

687 in the context of NASA’s ECOSTRESS mission [46]. It allows us to quantify the ability of  
688 inferences based on remote sensing retrievals to capture spatial features as well as individual,  
689 per-pixel behavior. It also presents new computational and modeling challenges because of  
690 high dimensionality and massive data set size. In the mean time, we continue work to improve  
691 the characterization of sounding-by-sounding uncertainty quantification for operational remote  
692 sensing missions like OCO-2.

693 **Appendix A. Generating the synthetic true state vector ensemble.** This appendix gives  
694 additional details of how we generate realizations of  $\mathbf{X}_{\text{land}}^{\text{sim}}$ . The state vector includes a diverse  
695 collection of atmospheric, surface, and instrument properties. These include the vertical  
696 profile of CO<sub>2</sub>, scaling factors for temperature and water vapor, surface pressure, aerosol  
697 concentration and vertical position information, surface albedo, solar-induced fluorescence  
698 (SIF), and observation wavelength offsets [22]. Due to this combination of constituents, actual  
699 OCO-2 retrievals are a logical source for reference data to inform the simulations. We assemble  
700 OCO-2 retrieval products for the region-week combinations represented in our templates. We  
701 make a few modifications to the template sets for realism and pragmatism. First, the OCO-2  
702 retrievals of aerosol amounts have not been reliably validated [33], so we replace them with  
703 values from the MERRA-2 reanalysis [40]. The MERRA-2 aerosol products are available  
704 globally every three hours at a grid spacing of 0.5° latitude × 0.625 longitude. We match  
705 each OCO-2 retrieval to the closest MERRA-2 location and time. The ergodic assumption  
706 is modified for the state vector elements corresponding to surface pressure and instrument  
707 dispersion. The variability across a template for these components is partially predictable  
708 due to changes in elevation, meteorology, and instrument calibration. This knowledge is  
709 captured in a variable retrieval prior mean for these quantities, so we subtract the prior mean  
710 vector used in the operational OE retrieval from the retrieved state for these elements in our  
711 template sets. A value for a reference sounding is added back when the simulation is executed,  
712 as discussed in Section 4.1.2

713 We filter out any OCO-2 soundings for which the retrieval algorithm did not converge to  
714 a solution within the maximum number of iterations allowed. This information is provided  
715 in a variable called `outcome_flag` that is provided in the data product. We also filter out any  
716 soundings for which an additional quality indicator, called `warn_level` [28], does not have value  
717 less than or equal to 15. Finally, because some state vector elements are on different scales,  
718 those elements with variability on the order of 10<sup>-4</sup> or less are multiplied by 1000 in order to  
719 avoid problems with covariance matrix inversion later. This rescaling is undone after fitting  
720 the mixture model.

721 To generate the synthetic truth ensembles for each land template, we fit a Gaussian  
722 mixture model,  $\tilde{P}_r$ ,  $r = \text{L1}, \dots, \text{L11}$  using the `densityMclust` function in R’s `mclust` package  
723 [47]. The procedure is described in Section 3.2. Here, we set the maximum number of  
724 components in the mixture to 15, which is the largest number that we felt we could legitimately  
725 interpret scientifically, and reduce the dimension of the input state vectors by projecting them  
726 into the space of the leading principal components (see Section 3.2) using a threshold of  
727  $\gamma = .95$ . Both choices are based on balancing the quality of the GMM fit against the time  
728 it takes to fit the models. We perform this step *only* if the number of screened data vectors  
729 in the template is at least ten times the number of leading eigenvectors used for dimension

730 reduction. We abandon any template strata which do not meet this criterion. Denote the  
731 simulation “marginal distribution” for template  $r$  by,

$$732 \quad (A.1) \quad \tilde{P}_r = \text{GMM} \left( \tilde{K}_r^{\text{sim}}, \left\{ \tilde{\boldsymbol{\eta}}_{rk}, \tilde{\boldsymbol{\Omega}}_{rk}, \tilde{P}_{rk} \right\}_{k=1}^{\tilde{K}_r^{\text{sim}}} \right), \quad r = \text{L1}, \dots, \text{L11},$$

733  
734 where all mean vectors and covariance matrices are on the original physical scale.

735 **Appendix B. The forward function and its parameters.** The OCO-2 full-physics (FP)  
736 forward model includes three key modules that we describe briefly, and we refer the reader  
737 to [2] for additional details. The FP forward model first solves the equation of radiative  
738 transfer (RT) at fine spectral resolution. Some discussion of the transformation from state  
739 vector elements to model inputs is provided by [19]. Next, the wavelength-dependence of the  
740 solar spectrum is applied to the solution. The final step of the FP model evaluation is the  
741 convolution of the fine-resolution spectral response with the OCO-2 instrument line shape  
742 (ILS), or spectral response function, and the result is the forward model evaluation for a  
743 generic synthetic state vector  $\mathbf{X}^{\text{sim}}$ ,

$$744 \quad (B.1) \quad \mathbf{Y}_0^{\text{sim}} = F_1(\mathbf{X}^{\text{sim}}, \mathbf{b}_1),$$

745 where  $\mathbf{b}_1$  are forward model parameters that are also used in the retrieval algorithm.

746 At least one special circumstance of the simulation experiment sets it apart from the cir-  
747 cumstances of the actual observing system: the simulated state vectors do not have latitudes  
748 and longitudes associated with them. Thus, they have no location information other than that  
749 they were generated by a synthetic marginal distribution distribution associated with a tem-  
750 plate. Actual forward model evaluations are dependent on geographic location because this  
751 determines their observing geometry, including sun angle and other details of the observing  
752 configuration. To overcome this problem, we use the observing geometry of a template “ref-  
753 erence sounding” for all forward model evaluations of synthetic state vectors drawn from the  
754 template’s synthetic marginal distribution. Reference soundings are typically located near the  
755 geographic center of the template so as to be generally representative of observing conditions.

756 The observing geometry parameters are some of the components of the parameter vector  
757  $\mathbf{b}_1$ . Other components include wavelength-specific parameters that describe aerosol scattering  
758 and gas absorption properties. Similarly, the instrument line shape (ILS) and solar spectrum  
759 are represented by parameters varying with wavelength that are subject to uncertainty. Con-  
760 nor et al. [5] assess the linear sensitivity of the operational OCO-2 retrieval to several of these  
761 parameters individually under a range of geophysical conditions. As we describe in 4.1.4, we  
762 represent forward model misspecification and parameter uncertainty collectively through an  
763 additive model discrepancy in our simulation framework.

764 **Appendix C. Estimation of model discrepancy parameters.** This appendix outlines  
765 our procedure for estimating the parameters of the model discrepancy distribution introduced  
766 in Section 4.1.4. The definition of model discrepancy is the difference between the true and  
767 modeled radiances due only to the difference between  $F_0(\cdot, \mathbf{b}_0)$  and  $F_1(\cdot, \mathbf{b}_1)$ , both evaluated  
768 at the true state,  $\mathbf{X}$ ,  
769

$$770 \quad \delta^{\text{sim}} = F_0(\mathbf{X}, \mathbf{b}_0) - F_1(\mathbf{X}, \mathbf{b}_1).$$

772 However, we only have access to  $F_1(\hat{\mathbf{X}}, \mathbf{b}_1)$ , which motivates the approximation,

$$773 \quad (C.1) \quad \delta^{\text{sim}} \approx F_0(\mathbf{X}, \mathbf{b}_0) - F_1(\hat{\mathbf{X}}, \mathbf{b}_1) - \left[ F_1(\mathbf{X}^{\text{sim}}, \mathbf{b}_1) - F_1(\hat{\mathbf{X}}^{\text{sim}}, \mathbf{b}_1) \right].$$

775 Let  $\mathbf{Y} \equiv F_0(\mathbf{X}, \mathbf{B}_0) + \epsilon$ , and  $\hat{\mathbf{Y}} \equiv F_1(\hat{\mathbf{X}}, \mathbf{b}_1)$ . The quantity  $(\mathbf{Y} - \hat{\mathbf{Y}})$  is the spectral residual,  
776 and is routinely produced as part of the retrieval process. The term in the square brackets  
777 can be computed from a simulation with no model discrepancy, where the noiseless forward  
778 model evaluation is readily available. The discrepancy can be written,

$$779 \quad \delta^{\text{sim}} \approx (\mathbf{Y} - \epsilon - \hat{\mathbf{Y}}) - (\mathbf{Y}_0^{\text{sim}} - \hat{\mathbf{Y}}^{\text{sim}}),$$

$$780 \quad \delta^{\text{sim}} + \epsilon \approx (\mathbf{Y} - \epsilon - \hat{\mathbf{Y}} + \epsilon) - (\mathbf{Y}_0^{\text{sim}} - \hat{\mathbf{Y}}^{\text{sim}}),$$

$$781 \quad (C.2) \quad = (\mathbf{Y} - \hat{\mathbf{Y}}) - (\mathbf{Y}_0^{\text{sim}} - \hat{\mathbf{Y}}^{\text{sim}}).$$

783 Therefore the sum of the discrepancy and noise can be approximated with the operational  
784 spectral residuals and simulation forward model evaluations. Taking the expectation and  
785 variance of  $\delta^{\text{sim}} + \epsilon$  facilitates estimation of  $\tilde{\boldsymbol{\mu}}_\delta$  and  $\tilde{\boldsymbol{\Sigma}}_\delta$ .

$$786 \quad \mathbb{E}(\delta^{\text{sim}} + \epsilon) \approx \mathbb{E}(\mathbf{Y} - \hat{\mathbf{Y}}) - \mathbb{E}(\mathbf{Y}_0^{\text{sim}} - \hat{\mathbf{Y}}^{\text{sim}}),$$

$$787 \quad (C.3) \quad \tilde{\boldsymbol{\mu}}_\delta + \mathbf{0} \approx \frac{1}{N} \sum_{n=1}^N (\mathbf{Y}_n - \hat{\mathbf{Y}}_n) - \frac{1}{M} \sum_{m=1}^M (\mathbf{Y}_{0,m}^{\text{sim}} - \hat{\mathbf{Y}}_m^{\text{sim}}),$$

789 where  $n = 1, \dots, N$  indexes actual OCO-2 retrievals in the template-week being studied, and  
790  $m = 1, \dots, M$  indexes trials of the simulation for that template-week. For the variance, we  
791 assume that the discrepancy and measurement noise are uncorrelated. Further, the spectral  
792 residuals from the actual OCO-2 retrievals are independent of the forward model evaluations  
793 from the simulation, by construction. Then,

$$794 \quad \text{cov}(\delta^{\text{sim}} + \epsilon) \approx \widehat{\text{cov}}(\mathbf{Y} - \hat{\mathbf{Y}}) + \widehat{\text{cov}}(\mathbf{Y}_0^{\text{sim}} - \hat{\mathbf{Y}}^{\text{sim}}),$$

$$795 \quad \tilde{\boldsymbol{\Sigma}}_\delta + \boldsymbol{\Sigma}_\epsilon \approx \widehat{\text{cov}}(\mathbf{Y} - \hat{\mathbf{Y}}) + \widehat{\text{cov}}(\mathbf{Y}_0^{\text{sim}} - \hat{\mathbf{Y}}^{\text{sim}}),$$

$$796 \quad (C.4) \quad \tilde{\boldsymbol{\Sigma}}_\delta \approx \widehat{\text{cov}}(\mathbf{Y} - \hat{\mathbf{Y}}) + \widehat{\text{cov}}(\mathbf{Y}_0^{\text{sim}} - \hat{\mathbf{Y}}^{\text{sim}}) - \boldsymbol{\Sigma}_\epsilon,$$

798 where  $\widehat{\text{cov}}(\mathbf{Y} - \hat{\mathbf{Y}})$  and  $\widehat{\text{cov}}(\mathbf{Y}_0^{\text{sim}} - \hat{\mathbf{Y}}^{\text{sim}})$  are suitable empirical estimates of the covariance  
799 matrices of the spectral residuals and simulation forward model evaluations, respectively.  
800 We have found that outliers are often present in the spectral residuals, so we implement  
801 an estimate that combines a rank correlation matrix with robust estimates of the standard  
802 deviations for individual wavelengths. In addition, there is no guarantee that the right-hand  
803 side of Equation (C.4) yields a positive definite matrix, particularly when the variability of  
804 the model discrepancy is similar to or smaller than the measurement noise. To remedy this,  
805 we simulate model discrepancy with a low-rank approximation by retaining only the leading  
806 principal components.

807 **Acknowledgments.** We would like to thank the Orbiting Carbon Observatory-2 Project  
808 for sponsoring this work, and Noel Cressie, Annmarie Eldering, Maggie Johnson, Mikael  
809 Kuusela, Mike Turmon, and Jouni Susiluoto for helpful discussions and insights. We also  
810 appreciate technical assistance from Dejian Fu and James McDuffie.

811 ©2019 California Institute of Technology.

812

## REFERENCES

- 813 [1] A. AGHAKOUCHAK, N. NASROLLAI, AND E. HABIB, *Accounting for uncertainties of the TRMM satellite*  
814 *estimates*, Remote Sensing, (2009), pp. 606–619, <https://doi.org/10.3390/rs1030606>.
- 815 [2] H. BOESCH, L. BROWN, R. CASTANO, M. CHRISTI, B. CONNOR, D. CRISP, A. ELDERING, B. FISHER,  
816 C. FRANKENBERG, M. GUNSON, R. GRANAT, J. MCDUFFIE, C. MILLER, V. NATRAJ, D. O'BRIEN,  
817 C. O'DELL, G. OSTERMAN, F. OYAFUSO, V. PAYNE, I. POLONSKI, M. SMYTH, R. SPURR,  
818 D. THOMPSON, AND G. TOON, *Orbiting Carbon Observatory-2 Level 2 Full Physics Algorithm*  
819 *Theoretical Basis Document*, Jet Propulsion Laboratory, March 2015. JPL document OCO D-55207.
- 820 [3] J. BRYNJARSDÓTTIR, J. HOBBS, A. BRAVERMAN, AND L. MANDRAKE, *Optimal estimation versus MCMC*  
821 *for CO<sub>2</sub> retrievals*, Journal of Agricultural, Biological, and Environmental Statistics, 23 (2018),  
822 pp. 297–316, <https://doi.org/10.1007/s13253-018-0319-8>.
- 823 [4] S. CHANDRASEKHAR, *Radiative Transfer*, Dover Publications, Inc., New York, 1960.
- 824 [5] B. CONNOR, H. BOSCH, J. MCDUFFIE, T. TAYLOR, D. FU, C. FRANKENBERG, C. O'DELL, V. H. PAYNE,  
825 M. GUNSON, R. POLLOCK, J. HOBBS, F. OYAFUSO, AND Y. JIANG, *Quantification of uncertainties*  
826 *in OCO-2 measurements of XCO<sub>2</sub>: simulations and linear error analysis*, Atmospheric Measurement  
827 Techniques, 9 (2016), pp. 5227–5238, <https://doi.org/10.5194/amt-9-5227/2016>.
- 828 [6] N. CRESSIE, *Mission CO<sub>2</sub>ntrol: A statistical scientist's role in remote sensing of atmospheric carbon*  
829 *dioxide*, Journal of the American Statistical Association, 113 (2018), pp. 152–168, [https://doi.org/](https://doi.org/10.1080/01621459.2017.1419136)  
830 [10.1080/01621459.2017.1419136](https://doi.org/10.1080/01621459.2017.1419136).
- 831 [7] N. CRESSIE AND R. WANG, *Statistical properties of the state obtained by solving a nonlinear multivariate*  
832 *inverse problem*, Applied Stochastic Models in Business and Industry, 29 (2013), pp. 424–438, [https://doi.org/](https://doi.org/10.1002/asmb.1946)  
833 [10.1002/asmb.1946](https://doi.org/10.1002/asmb.1946).
- 834 [8] N. CRESSIE, R. WANG, M. SMYTH, AND C. MILLER, *Statistical bias and variance for the regularized*  
835 *inverse problem: Application to space-based atmospheric CO<sub>2</sub> retrievals*, Journal of Geophysical Re-  
836 search: Atmospheres, 121 (2016), pp. 5526–5537, <https://doi.org/10.1002/2015JJD024353>.
- 837 [9] D. CRISP, *Measuring atmospheric carbon dioxide from space with the Orbiting Carbon Observatory-2*  
838 *(OCO-2)*, in Earth Observing Systems, vol. 9607, SPIE, 2014, <https://doi.org/10.1117/12.2187291>.
- 839 [10] A. DAVISON AND D. HINKLEY, *Bootstrap Methods and Their Application*, Cambridge University Press,  
840 Cambridge, UK, 1997.
- 841 [11] R. D. DE VEAUX, *Mixture of linear regressions*, Computational Statistics and Data Analysis, 8 (1989),  
842 pp. 227–245, [https://doi.org/10.1016/0167-9473\(89\)90043-1](https://doi.org/10.1016/0167-9473(89)90043-1).
- 843 [12] B. EFRON AND R. J. TIBSHIRANI, *Introduction to the Bootstrap*, Chapman and Hall, Boca Raton, FL,  
844 1994.
- 845 [13] A. ELDERING, C. W. O'DELL, P. O. WENNING, D. CRISP, M. GUNSON, C. VIATTE, C. AVIS,  
846 A. BRAVERMAN, ET AL., *The Orbiting Carbon Observatory-2: First 18 months of science data*  
847 *products*, Atmospheric Measurement Techniques, 10 (2017), pp. 549–563, [https://doi.org/10.5194/](https://doi.org/10.5194/amt-10-549-2017)  
848 [amt-10-549-2017](https://doi.org/10.5194/amt-10-549-2017).
- 849 [14] A. ELDERING, G. OSTERMAN, R. POLLOCK, R. LEE, R. ROSENBERG, F. OYAFUSO, D. CRISP, L. CHAP-  
850 SKY, AND R. GRANAT, *Orbiting Carbon Observatory (OCO-2) Level 1B Algorithm Theoretical Basis*,  
851 Jet Propulsion Laboratory, 2017. JPL document OCO D-55206.
- 852 [15] A. ELDERING, T. E. TAYLOR, C. W. O'DELL, AND R. PAVLICK, *The OCO-3 mission: measurement*  
853 *objectives and expected performance based on 1 year of simulated data*, Atmospheric Measurement  
854 Techniques, 12 (2019), <https://doi.org/10.5194/amt-12-2341-2019>.
- 855 [16] C. FRALEY AND A. E. RAFTERY, *Model-Based Clustering, Discriminant Analysis, and Density Estima-*  
856 *tion*, Journal of the American Statistical Association, 97 (2002).
- 857 [17] K. R. GURNEY AND CO AUTHORS, *Towards robust regional estimates of CO<sub>2</sub> sources and sinks using*  
858 *atmospheric transport models*, Nature, 415 (2002).
- 859 [18] H. HAARIO, M. LAINE, M. LEHTINEN, E. SAKSMAN, AND J. TAMMINEN, *Markov chain Monte Carlo*  
860 *methods for high dimensional inversion in remote sensing*, Journal of the Royal Statistical Society,  
861 Series B, 66 (2004).
- 862 [19] J. HOBBS, A. BRAVERMAN, N. CRESSIE, R. GRANAT, AND M. GUNSON, *Simulation-based uncertainty*  
863 *quantification for estimating atmospheric CO<sub>2</sub> from satellite data*, Journal on Uncertainty Quantifi-  
864 cation, 5 (2017), pp. 956–985, <https://doi.org/10.1137/16M1060765>.

- 865 [20] G. C. HULLEY, C. G. HUGHES, AND S. J. HOOK, *Quantifying uncertainties in land surface temperature*  
866 *and emissivity retrievals from ASTER and MODIS thermal infrared data*, *Journal of Geophysical*  
867 *Research*, 117 (2012), <https://doi.org/10.1029/2012JD018506>.
- 868 [21] S. ILLINGWORTH, J. REMEDIOS, H. BOESCH, D. MOORE, H. SEMBHI, A. DUDHIA, AND J. WALKER,  
869 *ULIRS, an optimal estimation retrieval scheme for carbon monoxide using IASI spectral radiances:*  
870 *sensitivity analysis, error budget and simulations*, *Atmospheric Measurement Techniques*, 4 (2011),  
871 p. 269288, <https://doi.org/10.5194/amt-4-269-2011>.
- 872 [22] S. S. KULAWIK, C. O'DELL, R. R. NELSON, AND T. E. TAYLOR, *Validation of OCO-2 error analysis*  
873 *using simulated retrievals*, *Atmospheric Measurement Techniques*, 12 (2019), [https://doi.org/10.5194/](https://doi.org/10.5194/amt-12-5317-2019)  
874 [amt-12-5317-2019](https://doi.org/10.5194/amt-12-5317-2019).
- 875 [23] M. KUUSELA AND V. M. PANARETOS, *Statistical unfolding of elementary particle spectra: empirical*  
876 *Bayes estimation and bias-corrected uncertainty quantification*, *The Annals of Statistics*, 9 (2015),  
877 <https://doi.org/10.1214/15-AOAS857>.
- 878 [24] O. LAMMINPÄÄ, J. HOBBS, J. BRYNJARSDÓTTIR, M. LAINE, A. BRAVERMAN, H. LINDQVIST, AND  
879 J. TAMMINEN, *Accelerated MCMC for satellite-based measurements of atmospheric CO<sub>2</sub>*, *Remote*  
880 *Sensing*, 11 (2019), <https://doi.org/10.3390/rs11172061>.
- 881 [25] N. LIVESEY, W. V. SNYDER, W. READ, AND P. WAGNER, *Retrieval algorithms for the EOS Microwave*  
882 *limb sounder (MLS)*, *Transactions on Geoscience and Remote Sensing*, 44 (2006), [https://doi.org/10.](https://doi.org/10.1109/TGRS.2006.872327)  
883 [1109/TGRS.2006.872327](https://doi.org/10.1109/TGRS.2006.872327).
- 884 [26] P. MA, E. KANG, A. BRAVERMAN, AND H. NGUYEN, *Spatial statistical downscaling for constructing high-*  
885 *resolution nature runs in global observing system simulation experiments*, *Technometrics*, 61 (2017),  
886 pp. 322–340, <https://doi.org/10.1080/00401706.2018.1524791>.
- 887 [27] V. MAGGIONI, M. R. SAPIANO, R. F. ADLER, Y. TIAN, AND H. G. J., *An error model for uncertainty*  
888 *quantification in high-time-resolution precipitation products*, *Journal of Hydrometeorology*, 15 (2014),  
889 <https://doi.org/10.1175/JHM-D-13-0112.1>.
- 890 [28] L. MANDRAKE, C. FRANKENBERG, C. O'DELL, G. OSTERMAN, P. WENNBERG, AND D. WUNCH, *Semi-*  
891 *autonomous sounding selection for OCO-2*, *Atmospheric Measurement Techniques, Discussions*, 6  
892 (2013), pp. 5881–5922, <https://doi.org/10.5194/amt-d-6-5881-2013>.
- 893 [29] G. MCLACHLAN AND D. PEEL, *Finite Mixture Models*, *Wiley Series in Probability and Statistics*, New  
894 York, 2000.
- 895 [30] C. A. MEARS, F. J. WENTZ, P. THORNE, AND D. BERNIE, *Assessing uncertainty in estimates of at-*  
896 *mospheric temperature changes from MSU and AMSU using a Monte Carlo estimation technique*,  
897 *Journal of Geophysical Research*, 116 (2011), <https://doi.org/10.1029/2010JD014954>.
- 898 [31] C. J. MERCHANT, F. PAUL, T. POPP, M. ABLAIN, S. BONTEMPS, P. DEFOURNY, H. RAINER,  
899 T. LAVERGNE, A. LAENG, G. DE LEEUW, J. MITTAZ, C. POULSEN, A. C. POVEY, M. REUTER,  
900 S. SATHYENDRANATH, S. SANDVEN, V. F. SOFIEVA, AND W. WAGNER, *Uncertainty information*  
901 *in climate data records from Earth observation*, *Earth System Science Data*, 9 (2017), pp. 511–527,  
902 <https://doi.org/10.5194/essd-9-511-2017>.
- 903 [32] NATIONAL RESEARCH COUNCIL, COMMITTEE ON MATHEMATICAL FOUNDATIONS OF VERIFICATION, VAL-  
904 IDATION, AND UNCERTAINTY QUANTIFICATION, *Assessing the Reliability of Complex Models: Mathe-*  
905 *matical and Statistical Foundations of Verification, Validation, and Uncertainty Quantification*, The  
906 National Academies Press, Washington, DC, 2012.
- 907 [33] R. R. NELSON AND C. W. O'DELL, *The impact of improved aerosol priors on near-infrared measurements*  
908 *of carbon dioxide*, *Atmospheric Measurement Techniques*, 12 (2019), pp. 1495–1512, [https://doi.org/](https://doi.org/10.5194/amt-12-1495-2019)  
909 [10.5194/amt-12-1495-2019](https://doi.org/10.5194/amt-12-1495-2019).
- 910 [34] C. W. O'DELL, A. ELDERING, P. O. WENNBERG, D. CRISP, M. R. GUNSON, ET AL., *Improved retrievals*  
911 *of carbon dioxide from the Orbiting Carbon Observatory-2 with the version 8 ACOS algorithm*, *Atmo-*  
912 *spheric Measurement Techniques*, 11 (2018), pp. 6539–6576, <https://doi.org/10.5194/amt-6539-2018>.
- 913 [35] P. K. PATRA, D. CRISP, J. W. KAISER, D. WUNCH, T. SAEKI, K. ICHII, T. SEKIYA, P. O. WENNBERG,  
914 D. G. FEIST, D. F. POLLARD, D. W. T. GRIFFITH, V. A. VELAZCO, M. DE MAZIERE, M. K. SHA,  
915 C. ROEHL, C. ABHISHEK, AND K. ISHIJIMA, *The Orbiting Carbon Observatory (OCO-2) tracks 2–*  
916 *3 peta-gram increase in carbon release to the atmosphere during the 2014–2016 El Nino*, *Scientific*  
917 *Reports*, 7 (2017), <https://doi.org/10.1038/s41598-017-13459-0>.
- 918 [36] S. PLATNICK, K. G. MEYER, M. D. KING, G. WIND, N. AMARASINGHE, B. MARCHANT, G. T. ARNOLD,

- 919 Z. ZHANG, P. A. HUBANKS, R. E. HOLZ, P. YANG, W. L. RIDGWAY, AND J. RIEDI, *The MODIS*  
920 *cloud optical and microphysical products: Collection 6 updates and examples from Terra and Aqua*,  
921 IEEE Transactions on Geosciences and Remote Sensing, 55 (2017), pp. 502–525, <https://doi.org/10.1109/TGRS.2016.2610522>.  
922
- [37] S. PLATNICK, R. PINCUS, B. WIND, M. D. KING, M. A. GRAY, AND P. HUBANKS, *An initial analysis*  
923 *of the pixel-level uncertainties in global MODIS cloud optical thickness and effective particle size re-*  
924 *trievals*, in Passive Optical Remote Sensing of the Atmosphere and Clouds, IV, S. C. Tsay, T. Yakota,  
925 and M.-H. Ahn, eds., vol. 5652, SPIE, 2004, pp. 30–40, <https://doi.org/10.1117/12.578353>.  
926
- [38] D. J. POSSELT AND G. D. MACE, *MCMC-based assessment of the error characteristics of a surface-*  
927 *based combined radarpassive microwave cloud property retrieval*, Journal of Applied Meteorology and  
928 Climatology, (2014), <https://doi.org/10.1175/JAMC-D-13-0237.1>.  
929
- [39] A. POVEY AND R. GRANGER, *Known and unknown unknowns: uncertainty estimation in satellite remote*  
930 *sensing*, Atmospheric Measurement Techniques, 8 (2015), pp. 4699–4718, [https://doi.org/10.5194/](https://doi.org/10.5194/amt-8-4699-2015)  
931 [amt-8-4699-2015](https://doi.org/10.5194/amt-8-4699-2015).  
932
- [40] C. A. RANGLES, A. M. DA SILVA, V. BUCHARD, P. R. COLARCO, A. DARMENOV, R. GOVINDARAJU,  
933 A. SMIRNOV, B. HOLBEN, R. FERRARE, J. HAIR, Y. SHINOZUKA, AND C. J. FLYNN, *The MERRA-*  
934 *2 Aerosol Reanalysis, 1980 Onward. Part I: System Description and Data Assimilation Evaluation*,  
935 Journal of Climate, 30 (2017), pp. 6823–6850, <https://doi.org/10.1175/JCLI-D-16-0609.1>.  
936
- [41] C. RAO, *Linear Statistical Inference*, John Wiley and Sons, New York, 1973.  
937
- [42] C. D. RODGERS, *Retrieval of atmospheric temperature and composition from remote measurements of*  
938 *thermal radiation*, Reviews of Geophysics and Space Physics, 14 (1976).  
939
- [43] C. D. RODGERS, *Inverse Methods for Atmospheric Sounding, Theory and Practice*, World Scientific,  
940 Singapore, 2000.  
941
- [44] I. RYOICHI, S. NAKO, O. YOSHIFUMI, AND T. SHOICHI, *CO<sub>2</sub> retrieval performance of TANSO-FTS*  
942 *(TIR) sensor aboard greenhouse gases observing satellite (GOSAT)*, in 15th Symposium on High-  
943 Resolution Molecular Spectroscopy, vol. 6580, SPIE, 2006, pp. 253 – 258, [https://doi.org/10.1117/](https://doi.org/10.1117/12.724963)  
944 [12.724963](https://doi.org/10.1117/12.724963).  
945
- [45] J. SCHAFER, R. OPGEN-RHEIN, V. ZUBER, M. AHDESMAKI, D. SILVA, A. PEDRO, AND K. STRIMMER,  
946 *corpcor: Efficient estimation of covariance and (partial) correlation*, 2017, [https://CRAN.R-project.](https://CRAN.R-project.org/package=corpcor)  
947 [org/package=corpcor](https://CRAN.R-project.org/package=corpcor). R package version 1.6.9.  
948
- [46] D. SCHIMEL AND F. D. SCHNEIDER, *Flux towers in the sky: global ecology from space*, New Phytologist,  
949 224 (2019), <https://doi.org/10.1111/nph.15934>.  
950
- [47] L. SCRUGGA, M. FOP, T. B. MURPHY, AND A. E. RAFTERY, *mclust 5: clustering, classification and*  
951 *density estimation using Gaussian finite mixture models*, The R Journal, 8 (2016), pp. 205–233,  
952 <https://journal.r-project.org/archive/2017/RJ-2017-008/RJ-2017-008.pdf>.  
953
- [48] H. G. SUNG, *Gaussian mixture regression and classification*, PhD thesis, Rice University, 2004, <http://hdl.handle.net/1911/18710>.  
954
- [49] A. TARANTOLA, *Inverse Problem Theory and Methods for Model Parameter Estimation*, Society for In-  
955 *dustrial and Applied Mathematics*, Philadelphia, PA, 2005.  
956
- [50] D. R. THOMPSON, V. NATRAJ, R. O. GREEN, M. C. HELMLINGER, B.-C. GAO, AND M. L. EASTWOOD,  
957 *Optimal estimation for imaging spectrometer atmospheric correction*, Remote Sensing of Environment,  
958 216 (2018), pp. 355–373, <https://doi.org/10.1016/j.rse.2018.07.003>.  
959
- [51] Y. TIAN AND K. HARRISON, *Special issue: Uncertainties in Remote Sensing*, Remote Sensing, 9 (2017),  
960 <https://www.mdpi.com/journal/remotesensing/specialIssues/uncertaintiesRS>.  
961
- [52] J. WARNER, L. STROW, C. BARNET, L. SPARLING, G. DISKIN, AND G. SACHSE, *Improved agreement*  
962 *of airs tropospheric carbon monoxide products with other EOS sensors using optimal estimation re-*  
963 *trievals*, Atmospheric Chemistry and Physics, 10 (2010), <https://doi.org/10.5194/acp-10-9521-2010>.  
964
- [53] J. R. WORDEN, G. B. DORAN, S. KULAWIK, A. ELDERING, D. CRISP, C. FRANKENBERG, C. O’DELL,  
965 AND K. BOWMAN, *Evaluation and attribution of OCO-2 XCO<sub>2</sub> uncertainties*, Atmospheric Measure-  
966 *ment Techniques*, 10 (2017), pp. 2759–2771, <https://doi.org/10.5194/amt-10-2759-2017>.  
967
- [54] D. WUNCH, G. C. TOON, J.-F. L. BLAVIER, R. A. WASHENFELDER, J. NOTHOLT, B. J. CONNOR, D. W.  
968 GRIFFITH, V. SHERLOCK, AND P. O. WENBERG, *The Total Carbon Column Observing Network*,  
969 *Philosophical Transactions of the Royal Society, A*, 369 (2011), [https://doi.org/doi:10.1098/rsta.2010.](https://doi.org/doi:10.1098/rsta.2010.0240)  
970 [0240](https://doi.org/doi:10.1098/rsta.2010.0240).  
971  
972

- 973 [55] D. WUNCH, P. O. WENNBERG, G. OSTERMAN, B. FISHER, B. NAYLOR, C. M. ROEHL, C. O'DELL,  
974 L. MANDRAKE, C. VIATTE, M. KIEL, D. W. T. GRIFFITH, N. M. DEUSCHER, V. A. VELAZCO,  
975 J. NOTHOLT, T. WARNEKE, C. PETRI, M. DE MAZIERE, M. K. SHA, R. SUSSMANN, M. RETTINGER,  
976 D. POLLARD, J. ROBINSON, I. MORINO, O. UCHINO, F. HASE, T. BLUMENSTOCK, D. G. FEIST,  
977 S. G. ARNOLD, K. STRONG, J. MENDONCA, R. KIVI, P. HEIKKINEN, L. IRACI, J. PODOLSKE, P. W.  
978 HILLYARD, S. KAWAKAMI, M. K. DUBEY, H. A. PARKER, E. SEPULVEDA, O. E. GARCA, Y. TE,  
979 P. JESECK, M. R. GUNSON, D. CRISP, AND A. ELDERING, *Comparisons of the Orbiting Carbon*  
980 *Observatory-2 (OCO-2) XCO<sub>2</sub> measurements with TCCON*, *Atmospheric Measurement Techniques*,  
981 10 (2017), pp. 2209–2238, <https://doi.org/10.5194/amt-10-2209-2017>.  
982 [56] L. XIN, *China launches carbon-dioxide mission*, *Physics World*, 30 (2017).  
983 [57] D. YANG, H. ZHANG, Y. LIU, B. CHEN, Z. CAI, AND D. LU, *Monitoring carbon dioxide from space: Re-*  
984 *trieval algorithm and flux inversion based on GOSAT data and using CarbonTracker–China*, *Advances*  
985 *in Atmospheric Sciences*, 34 (2017), pp. 965–976, <https://doi.org/10.1007/s00376-017-6221-4>.